

Vážený a milý čtenáři.

V rukou držíš sborník studentských příspěvků již **14. Studentské vědecké konference fyziky pevných látek (SVK FPL 5)** každoročně pořádané Katedrou inženýrství pevných látek Fakulty jaderné a fyzikálně inženýrské Českého vysokého učení v Praze s podporou Studentského grantového systému SGS ČVUT v Praze.

Místem konání konference byl opět, tak jako v roce loňském, penzion Kamínek situovaný v Byňově poblíž Nových Hradů v jižních Čechách v termínu 23. - 25. září 2025.

Na letošní konferenci bylo presentováno celkem 16 příspěvků (11 studentských, 5 lektorských). Obsahová i formální kvalita přednesených studentských prezentací byla opět velmi dobrá, plně srovnatelná s úrovní, kterou můžeme vidět na "dospělých" akcích. Tradičně vysokou a motivující úroveň měly i diskuse následující po jednotlivých vystoupeních. Díky širokému tematickému záběru účastníků naší akce (pokrývajícímu řadu rozdílných oblastí: přípravu nových funkčních materiálů, difrakční metody charakterizace reálné struktury kovů, slitin a biologických makromolekul, fotonické a termoelektrické aplikace, počítačové simulace kondenzovaných látek a experimentální charakterizaci spektrálních vlastností) jsme byli, jako v předešlých letech, častými svědky heuristického efektu "progresivní interference idejí", při které byly podněty z jedné vědní oblasti přenášeny do jiné za vzniku nových nápadů - nové kvality - stimulující další výzkumné aktivity.

Úvodní slovo bych chtěl uzavřít poděkováním a pozváním.

- Děkuji všem přednášejícím a diskutujícím za jejich nenahraditelný odborný vklad, bez něhož by konference nemohla proběhnout.
- Členům organizačního výboru děkuji za perfektní zajištění všech potřebných nezbytností. Organizace konference běžela jako dobře namazaný a seřízený stroj, jehož přítomnost v pozadí věcí je klíčová, avšak stěží zaznamatelná.
- Děkuji též všem pracovníkům penzionu Kamínek, za jejich ochotu, vstřícnost a vysokou úroveň poskytovaných služeb.

Za kolektiv organizátorů SVK FPL

Ladislav Kalvoda

ISBN 978-80-01-07499-2

Structure parameters of additively manufactured AlSi10Mg alloy

Martin Endrych¹, Karel Trojan¹, Jiří Čapek¹, Radim Halama²

¹Department of Solid State Engineering, Faculty of Nuclear Sciences and Physical Engineering, Czech Technical University in Prague

²Faculty of Mechanical Engineering, VSB – Technical University of Ostrava

Abstract

Selective Laser Melting (SLM) technology, one of additive manufacturing methods, results in specific structure parameters, which can depend on the orientation of the products during fabrication. To examine structure parameters, specifically the residual stresses and crystallographic preferred orientation, of AlSi10Mg aluminium alloy samples, X-ray diffraction methods were used. Specimens with six different orientations relative to the building platform were prepared by SLM and investigated. It was found that the chosen orientation of the sample during SLM significantly affects the crystallographic preferred orientation and the residual stress state. The preferred crystallographic orientation or texture is directly linked to the printing direction.

Keywords: X-ray diffraction; AlSi10Mg; Selective Laser Melting; residual stress; texture.

Introduction

Selective laser melting (SLM) technology is one of the additive manufacturing (AM) methods. SLM is based on the gradual addition of layers of metal powder and the selective melting of each layer with a laser. These manufacturing processes are often able to meet demanding requirements for complex shapes, as well as shorten production times in many areas such as automotive, aerospace and medicine. [1]

The structure of materials produced in this way has specific characteristics that differ from conventionally processed materials. In particular, the microstructure is very fine and anisotropic primarily due to high temperature gradients. [2] This affects the properties of additively manufactured products. Important structural parameters that influence the so-called real structure of materials include residual stresses and crystallographic preferred orientation (texture). These parameters can be non-destructively determined using methods based on X-ray diffraction. [3]

The presence and character of residual stresses and texture in materials is known to influence the distribution and magnitude of physical quantities such as tensile strength or fatigue resistance. By correctly identifying these parameters, it is possible to adapt manufacturing processes and thereby modify the mechanical, electrical, or magnetic properties of the final products. [4, 5]

The aim of this research is to investigate residual stresses and crystallographic preferred orientation of AlSi10Mg samples prepared by SLM technology. Particular interest is given to the description of these parameters with respect to different orientations relative to the building platform.

Experiment

AlSi10Mg alloy cylindrical samples with a diameter of 10 mm from recycled powder were produced using a Renishaw AM400 device with the printing parameters: laser power 350 W, spot size 80 μm , layer thickness 30 μm , laser speed 1150 mm/s, and Meander printing strategy. No heat treatment was performed on the printed samples to maintain a fine-grained microstructure created by SLM technology. Samples are labeled 0° , 10° , 20° , 30° , 40° and 90° according to the inclination of their axial axis relative to the normal axis of the building platform.

In order to create a flat and sufficiently large surface on the samples for X-ray diffraction, the samples were machined by milling so that the width of the surface was at least 9 mm. Next, the samples were electrolytically polished to remove the layer of material affected by milling. *LectroPol 5 Struers* device was used with A2 electrolyte and a voltage of 13 V. The sample after both processes is shown in Figure 1. A section with a length of 10 mm and the width of the entire sample was polished. For the purpose of analyzing areas at the same distance from the building platform, the center of this polished area was selected at a distance of 15 ± 0.5 mm from the building platform for all samples except 90° . For the 90° , due to its orientation parallel to the platform during printing, the distance was only 4 ± 0.5 mm. The thickness of the removed layer of material for all samples was approximately 200 μm .

Residual stresses were determined by X-ray diffraction in *X'Pert PRO PANalytical* diffractometer and using the $\sin^2\psi$ method. The $\{311\}$ diffraction line of the aluminium phase was used. The measurements were done with chromium X-ray tube and in the directions x and y shown in Figure 1. The direction y corresponds to the main (axial) axis of the samples. Obtained diffraction data were analysed using *PANalytical Stress Plus* software. Preferred crystallographic orientations were determined by X-ray diffraction in *Empyrean PANalytical* diffractometer. In each sample, the plane defined by the x , y directions was analysed. Cobalt X-ray tube was used and $\{040\}$, $\{131\}$ and $\{222\}$ diffraction lines were examined. The *MATLAB* toolbox *MTEX* [6] was used to calculate complete pole figures and inverse pole figures from experimentally obtained pole figures.

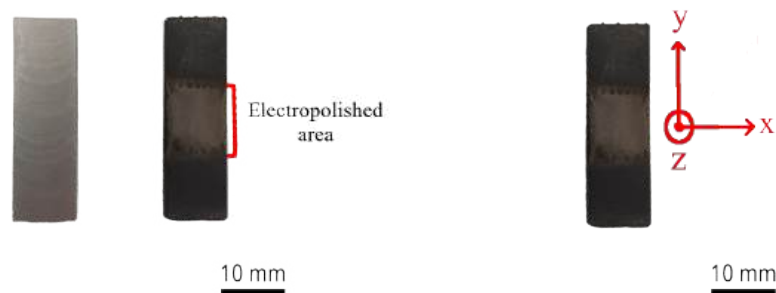


Figure 1: Sample after milling and electropolishing (left), definition of coordinates (right).

Results and Discussion

The values of normal residual stresses in examined directions x and y for all samples are shown in Figure 2. The values of shear residual stresses were also calculated. Compared to normal residual stresses, only small values of up to 11 MPa were present. This is due to a formation of residual stresses, particularly by temperature gradient.

For the y direction, the highest values of normal residual stresses (up to 60 MPa) were found in the sample printed with a 0° inclination. In this sample, the y direction is the printing direction, so the reason is presumably a greater temperature gradient in the y direction than in others. With increasing inclination, the y direction in individual samples deviates from the printing direction and the residual stress values decrease. For direction x , the values of normal residual stresses increase with increasing inclination relative to the values in the y direction.

The normal residual stress values in sample 90° are very low. This is probably a result of the large area in contact with the construction platform combined with the small distance between the examined area and the platform. Except for this sample, the values are positive, which implies tensile residual stresses.

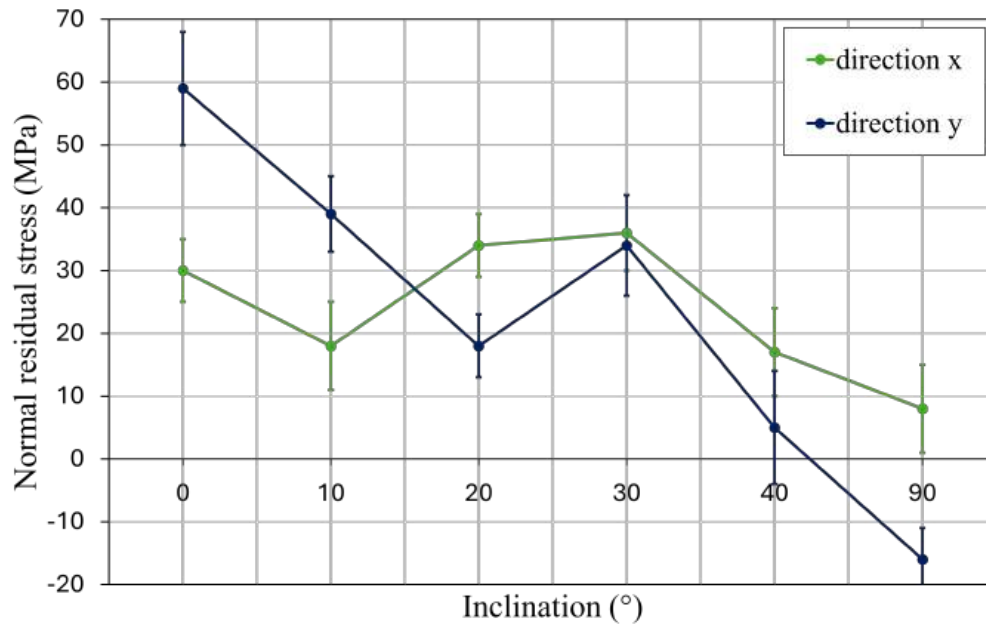


Figure 2: Normal residual stress values in the x and y directions for samples with inclinations of 0° , 10° , 20° , 30° , 40° and 90° .

The complete pole figures obtained for all analysed samples are shown in Figure 3. The colour scale is in multiples of a random distribution (m.r.d.). The $\{040\}$ planes have a noticeably stronger texture than the others. In sample 0° , the orientation of the $\{040\}$ planes in the y direction points to a texture with crystals oriented in a way that one of the $\langle 100 \rangle$ directions is parallel to the printing direction. As the inclination of the samples increases, corresponding inclinations can be observed in the pole figures, indicating the preservation of the preferred orientation in the direction of printing for all samples. The trend continues also in sample 90° , where the printing direction corresponds to the sample

z direction. The cubic component $\{001\}\langle 100\rangle$, which is common for fcc metals such as aluminium, is clearly visible. From the continuous bands in the $\{222\}$ planes, more components composing the fiber $\langle 100\rangle$ are evident.

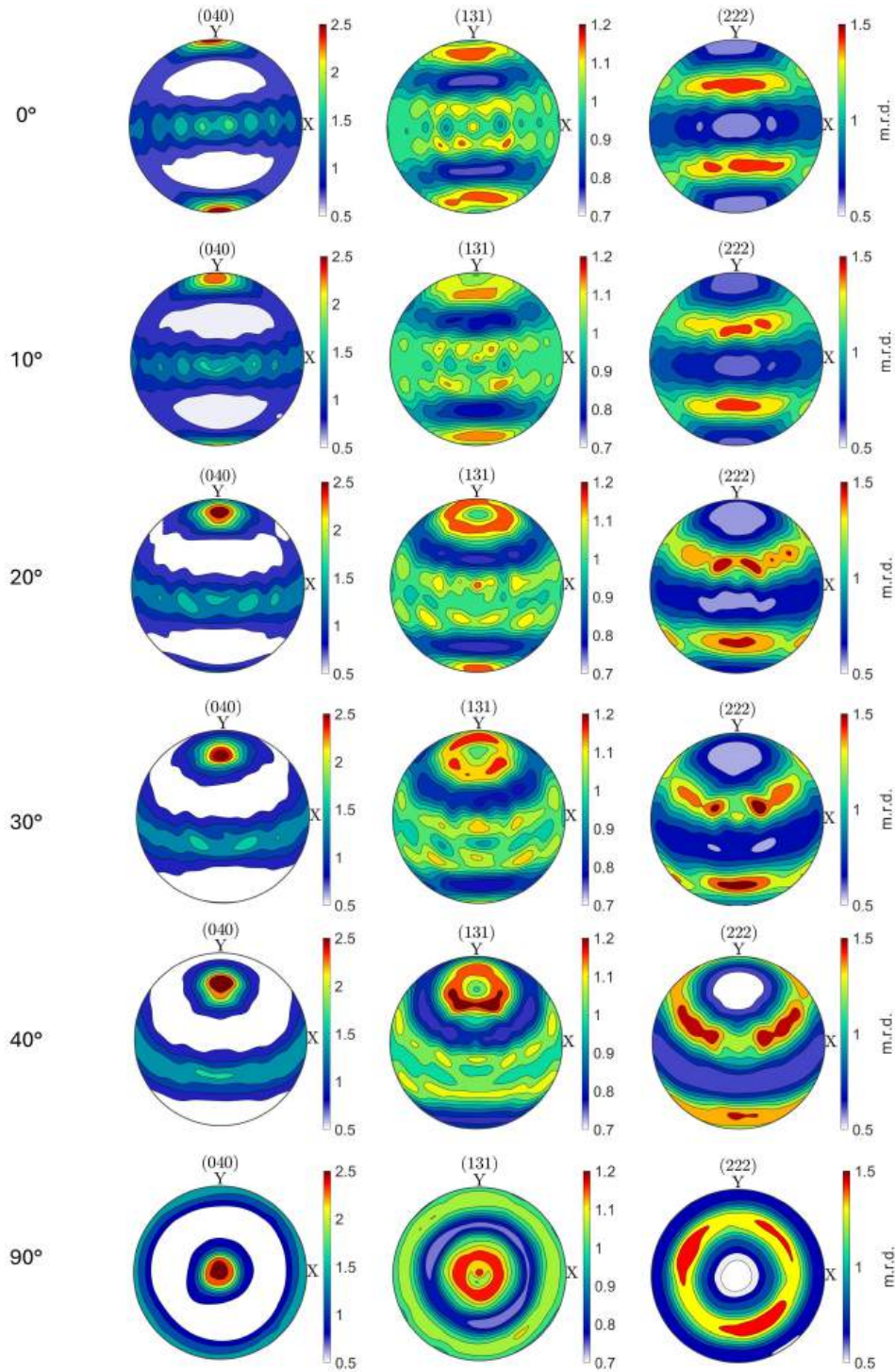


Figure 3: Complete pole figures of $\{040\}$, $\{131\}$ and $\{222\}$ diffraction lines for samples with inclinations of 0° , 10° , 20° , 30° , 40° and 90° .

Figure 4 shows the inverse pole figures of sample 0° along the x , y , and z sample directions. The sample has strong $\langle 100 \rangle$ fibrous texture in the y direction, that is in the printing direction. In the x and z directions, texture is present with much lower m.r.d. Together with the discussed preservation of the preferred orientation in the direction of printing for all samples (see Figure 3), it can be stated that the $\langle 100 \rangle$ fibrous texture in the printing direction occurs in all the examined samples.

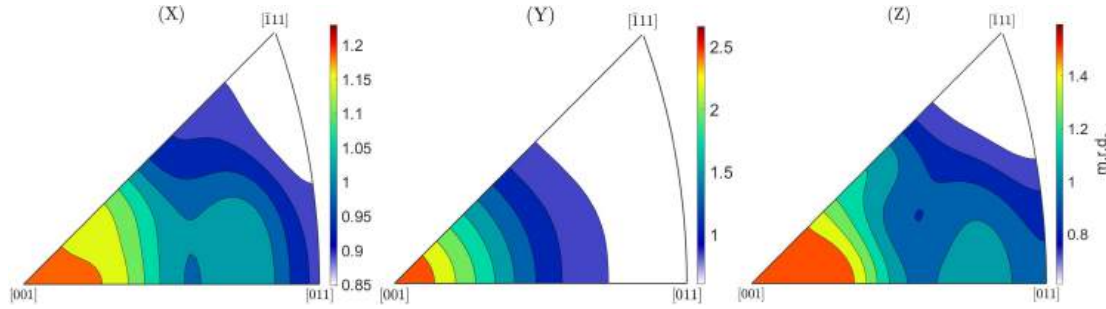


Figure 4: Inverse pole figures for all three directions x , y , z in sample 0° .

The dependence of the normal residual stress values in the y direction on multiples of a random distribution of the crystallographic direction $\langle 100 \rangle$ for the sample y direction is shown in Figure 5. An increase in normal residual stress values can be observed with an increasing number of crystallographic directions $\langle 100 \rangle$ oriented in the direction y of the sample in which the residual stress is examined. Deviations from this trend show samples with the inclination of 30° and 90° . In sample 90° , the likely reason is the previously discussed combination of a large contact area with the building platform and a small distance between the examined area and the platform. For sample 30° , we will attempt to clarify the reason for this deviation in further research. The reason for the correlation between m.r.d. and residual stresses will also be the subject of future research.

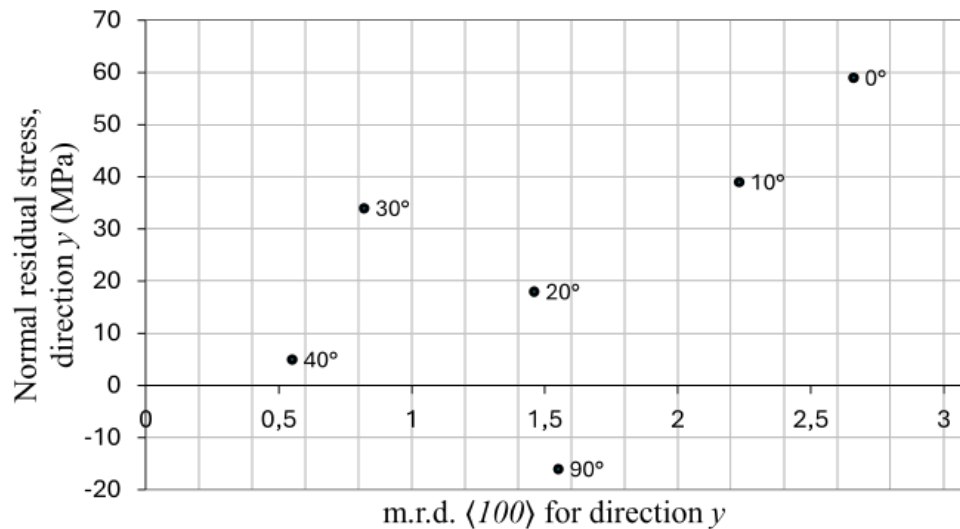


Figure 5: Values of normal residual stresses in the y direction of the samples with inclinations of 0° , 10° , 20° , 30° , 40° and 90° in dependence on m.r.d. $\langle 100 \rangle$ for the y direction.

Conclusions

Residual stresses and preferred crystallographic orientations of six AlSi10Mg samples with different inclination were analysed using X-ray diffraction. Small compressive and tensile residual stress values were found in the sample with the main axis parallel to the building platform. In the remaining samples, tensile normal residual stresses and small shear residual stresses were found in all cases. With increasing inclination from the axis perpendicular to the platform, a gradual decrease in normal residual stresses was found in the direction of the main axis of the samples. In the direction perpendicular to the main axis, a relative increase in residual stress values was found with increasing inclination compared to the values in the direction of the main axis. The results of crystallographic preferred orientation (texture) showed that a fibrous texture $\langle 100 \rangle$ forms in the samples in the direction of printing, regardless of the orientation of the sample. Also, the formation of this fibrous texture was compared with the residual stress state within the samples. Along the $\langle 100 \rangle$ fiber, the residual stress values are highest, and the decrease of values with increasing inclination of the main axis of the samples is consistent with the preservation of the preferred orientation in the printing direction. Since the orientation of the $\langle 100 \rangle$ fiber changes relative to the significant direction of the sample, further research should include potential influence on the mechanical properties of the samples.

References

- [1] J. Zhang, Y. Jung. *Additive manufacturing: Materials, processes, quantifications and applications*. Butterworth-Heinemann, Elsevier, 2018.
- [2] Q. Yan, B. Song, Y. Shi. Comparative study of performance comparison of AlSi10Mg alloy prepared by selective laser melting and casting. *Journal of Materials Science & Technology* **41**: 199-208, 2020. Available from: <https://doi.org/10.1016/j.jmst.2019.08.049>
- [3] I. Kraus, N. Ganev. *Technické aplikace difrakční analýzy*. Vydavatelství ČVUT, 2004.
- [4] G. Schajer. *Practical residual stress measurement methods*. Wiley, 2013.
- [5] O. Engler, V. Randle. *Introduction to Texture Analysis: Macrotecture, Microtexture, and Orientation Mapping*. CRC Press, Taylor & Francis Group, 2010.
- [6] F. Bachmann, R. Hielscher, H. Schaeben. Texture Analysis with MTEX – Free and Open Source Software Toolbox. *Solid State Phenomena* **160**: 63-68, 2010.

Acknowledgement

This work was supported by the Grant Agency of the Czech Technical University in Prague, grant No. SGS25/168/OHK4/3T/14.

Quantum-like Model of a Rat in a Maze

Aleksej Gaj^{1,2}, Miroslav Kárný²

¹Department of Solid State Engineering, Faculty of Nuclear Sciences and Physical Engineering, Czech Technical University in Prague

²Department of Adaptive Systems, Institute of Information Theory and Automation, Czech Academy of Sciences
aleksej.gaj@jfifi.cvut.cz

Abstract

Quantum mechanics (QM) provides a formal framework for modelling uncertainty and dynamic evolution in physical systems. While its mathematical structure is well established, its application beyond microscopic phenomena remains an area of active discussion. This work illustrates the axioms of QM in an intuitive, accessible way through a textbook-style example designed to parallel decision-making tasks.

The seemingly trivial setup raises questions about the interpretation and understanding of the underlying model. Though it offers no new contribution to QM theory, it serves as a conceptual bridge, demonstrating fundamental principles in a context involving a living organism. The approach may prove useful as a foundation for quantum-inspired models of decision-making and living systems. Links to contemporary interpretations of QM are also discussed.

Keywords: quantum mechanics, quantum-like model, expressing non-physical properties via quantum model, models of living matter.

Notation

Notation is introduced along the text, Table 1 just summarises key objects for later reference. Bra-ket notation [1] is used.

Object	Symbol/font used
Set	$\mathbf{A}, \mathbf{B}, \dots$
Set of real numbers	\mathbf{R}
Set of complex numbers	\mathbf{C}
Hilbert space	\mathcal{H}
Element from Hilbert space	$ \psi\rangle$
Operator on Hilbert space	$\hat{\mathbf{A}}, \hat{\mathbf{B}}, \dots$
Matrix representing the operator	$\mathbb{A}, \mathbb{B}, \dots$

Table 1: Mathematical objects used and their notion.

Introduction: Why rat? Why quantum?

Since we deal with quantum-like models for the tasks of dynamic decision-making (DM) [2], we came up with a simple example to illustrate how the postulates of quantum mechanics (QM) can be applied to a macro-scaled object, and what the technical and (more importantly) interpretational consequences are.

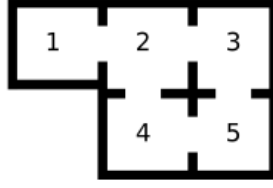


Figure 1: The box rat lives in.

Later became clear that such an example can serve as an environment for simulating more complex aspects of quantum theory.

1 The setup: Rat-in-the-box system

A closed, non-transparent box is divided into several rooms (see Fig.1). A rat is moving between those rooms in discrete steps (the position of the rat is represented by the number of the room). Only some rooms share a common door. The rat can only move through one door at a time (i.e. it takes her several steps to reach distant rooms). The rat is a completely normal rodent; she¹ cannot physically be in several rooms at once.

The rat starts in Room 1 (initial condition) and prefers to stay around Room 5, since it's the room where she is usually fed.

Let us model the rat-in-the-box system using quantum mechanics formalism. Since the box consists of 5 rooms, the state of the rat in the box can be represented² as a vector in a 5-dimensional Hilbert space \mathcal{H} :

$$\mathcal{H} = \text{span} \{ |\text{Room}_1\rangle, |\text{Room}_2\rangle, |\text{Room}_3\rangle, |\text{Room}_4\rangle, |\text{Room}_5\rangle \} \quad (1)$$

and the general state of the rat can be expressed as a linear combination:

$$|\psi(t)\rangle = c_1(t) |\text{Room}_1\rangle + c_2(t) |\text{Room}_2\rangle + c_3(t) |\text{Room}_3\rangle + c_4(t) |\text{Room}_4\rangle + c_5(t) |\text{Room}_5\rangle, \quad (2)$$

where $c_i(t) \in \mathbf{C}$ are complex coefficients satisfying the normalization condition:

$$\sum_{j=1}^5 |c_j(t)| = 1 \quad \text{for each } t \text{ fixed.} \quad (3)$$

Numeric representation of rooms (basis in \mathcal{H} represented by matrix $\mathbb{B}(0) \equiv \mathbb{I}$) could be:

$$\mathcal{H} = \text{span} \left\{ \begin{pmatrix} 1 \\ 0 \\ 0 \\ 0 \\ 0 \end{pmatrix}, \begin{pmatrix} 0 \\ 1 \\ 0 \\ 0 \\ 0 \end{pmatrix}, \begin{pmatrix} 0 \\ 0 \\ 1 \\ 0 \\ 0 \end{pmatrix}, \begin{pmatrix} 0 \\ 0 \\ 0 \\ 1 \\ 0 \end{pmatrix}, \begin{pmatrix} 0 \\ 0 \\ 0 \\ 0 \\ 1 \end{pmatrix} \right\}, \quad (4)$$

¹We refer to the rat in this story as *she/her*.

²This paper and this section especially demonstrate a complex approach using very simple algebra. That is the reason why trivial algebraic expressions are rewritten here in (unusually) detailed way.

where the j -th room is represented by $|\text{Room}_j\rangle \equiv |e_j\rangle$. Using (4), (2) reads:

$$|\psi(t)\rangle = c_1(t) \begin{pmatrix} 1 \\ 0 \\ 0 \\ 0 \\ 0 \end{pmatrix} + c_2(t) \begin{pmatrix} 0 \\ 1 \\ 0 \\ 0 \\ 0 \end{pmatrix} + c_3(t) \begin{pmatrix} 0 \\ 0 \\ 1 \\ 0 \\ 0 \end{pmatrix} + c_4(t) \begin{pmatrix} 0 \\ 0 \\ 0 \\ 1 \\ 0 \end{pmatrix} + c_5(t) \begin{pmatrix} 0 \\ 0 \\ 0 \\ 0 \\ 1 \end{pmatrix} = \begin{pmatrix} c_1(t) \\ c_2(t) \\ c_3(t) \\ c_4(t) \\ c_5(t) \end{pmatrix}. \quad (5)$$

Since the state is changing in time t , we assume coefficients of superposition are time dependent: $c_j(t)$. This can be expressed alternatively: the basis can be time dependent: $\mathbb{B}(t)$, i.e. due to time evolution the basis “rotates” while coefficients $c_j(t) = c_j$ remains constant.

2 Observable

Performing a measurement (an observation) means observing the rat’s position, i.e., the number of the room the rat is currently in $\{ '1', '2', '3', '4', '5' \}$. Corresponding observable is represented by Hermitian³ operator $\hat{A} : \mathcal{H} \rightarrow \mathcal{H}$ (in this case represented by matrix $\mathbb{A} \in \mathbf{R}^{5 \times 5}$). Spectrum of operator \hat{A} is $\sigma(\hat{A}) = \{1, 2, 3, 4, 5\}$, i.e. it is formed from a set of possible outcomes⁴.

2.1 Probability of observing the outcome

Since the rat’s movement is stochastic, we can only think about the probability of finding the rat in the j -th room if the system is in state $|\psi(t)\rangle$. According to Born’s rule, the probability is

$$P\left(\text{rat is in the } j\text{-th room} \mid |\psi(t)\rangle\right) = P\left(\alpha_j \mid |\psi(t)\rangle\right) = \left\| \hat{E}(\alpha_j) |\psi(t)\rangle \right\|^2, \quad (6)$$

where α_j is the j -th eigenvalue (representing the j -th outcome of an observation). $\hat{E}(\alpha_j) : \mathcal{H} \rightarrow \mathcal{H}$ is a projector to the j -th eigen-direction $|e_j\rangle$:

$$\hat{E}(\alpha_j) = |e_j\rangle \langle e_j|, \quad (7)$$

which suddenly gives a new meaning to the coefficients in (5):

$$P\left(\text{rat is in the } j\text{-th room} \mid |\psi(t)\rangle\right) = |c_j(t)|^2. \quad (8)$$

2.2 State update by an observation

The observation process itself influences the state of the rat-in-the-box system. State update can be done according to Lüders formula (also known as Projection postulate of QM [3]):

$$|\psi_{\alpha_j}(t)\rangle = \frac{\hat{E}(\alpha_j) |\psi(t)\rangle}{\left\| \hat{E}(\alpha_j) |\psi(t)\rangle \right\|}. \quad (9)$$

³Operator \hat{A} is Hermitian $\Leftrightarrow \hat{A} = \hat{A}^*$ (where in the case of matrix representation, star notes transposition and complex conjugation).

⁴This is also the reason why the observable is represented by a matrix of dimension 5: it has to have 5 different eigenvalues.

3 Time evolution

In QM setup time evolution is described via Schrödinger equation

$$\begin{cases} i\hbar \frac{d}{dt} |\psi(t)\rangle = \hat{H} |\psi(t)\rangle \\ |\psi(0)\rangle = |\psi_0\rangle \end{cases} \quad (10)$$

or alternatively by unitary operator $\hat{U} : \mathcal{H} \rightarrow \mathcal{H}$ in the following way:

$$\begin{cases} |\psi(t)\rangle = \hat{U}(t) |\psi(0)\rangle \\ |\psi(0)\rangle = |\psi_0\rangle, \end{cases} \quad (11)$$

where $|\psi_0\rangle \in \mathcal{H}$ is an initial condition and

$$\hat{U}(t) = \exp\left(-it \frac{1}{\hbar} \hat{H}\right). \quad (12)$$

In (10)–(12):

- i is a complex unit, \hbar is reduced Planck's constant, which can be omitted since it has no meaning in the considered setup
- t is time (\hat{U} is time-dependent)
- $\exp(\bullet)$ is exponential of an operator (in this case – exponential of a matrix⁵)
- \hat{H} is Hamiltonian of the system (an operator represented by a matrix).

The matrix representing \hat{H} is Hermitian and positive semi-definite (its eigenvalues are nonnegative). As a consequence, it is not necessary symmetric: its elements are complex numbers. Due to hermicity, the matrix is symmetric in real parts of its elements, but imaginary parts can differ.

For the scope of our rat-in-the-box setup, the Hamiltonian \hat{H} can be defined as follows.

- **Diagonal elements** represent the energy associated with a specific state, in our case, the “energy level” is associated with the rat being in a specific room. We can assign the following energies: $E_1 = 3$ for Room 1, $E_2 = 2$ for Room 2, $E_3 = 1$ for Room 3, $E_4 = 1$ for Room 4, $E_5 = 0$ for Room 5. This means that Room 1 is the least preferred one (by the rat) and Room 5 the most preferred one. It can be shown that only differences between energy levels matter (adding a constant to each element on the diagonal would not affect observation probabilities).
- **Off-diagonal elements** represents the coupling strength of the states, in the case of the rat, this tells how likely the rat is to go through the door (transition effort between two rooms). Mainly, this should reflect which rooms do not have a direct connection (for instance, Room 1 and Room 3 in Fig. 1).

⁵Exponential of a matrix is defined as

$$\exp(\mathbb{A}) = \sum_{j=0}^{+\infty} \frac{\mathbb{A}^j}{j!}. \quad (13)$$

Let us assign equal coupling strengths $a \in \mathbf{R}$:

$$\left\{ \begin{array}{l} |\psi(t)\rangle = \exp \left(\underbrace{-it \begin{pmatrix} 3 & a & 0 & 0 & 0 \\ a & 2 & a & a & 0 \\ 0 & a & 1 & 0 & a \\ 0 & a & 0 & 1 & a \\ 0 & 0 & a & a & 0 \end{pmatrix}}_{\hat{U}(t)} \right) |\psi(0)\rangle \\ |\psi(0)\rangle = |\psi_0\rangle. \end{array} \right. \quad (14)$$

Note: multiplying the Hamiltonian with a real number changes only time scale (i.e. $\hat{U}'(t) = \exp(-it(k\hat{H})) = \exp(-i(kt)\hat{H}) = \hat{U}(kt)$ for $\forall k \in \mathbf{k}$).

Since Hamiltonian expresses time dynamics of the rat-in-the-box system, it is expected that by a reasonable choice of elements in \hat{H} we can express the rat's aim – particularly her preference for the rooms (Room5 is the most preferred one, Room1 is the least preferred by her).

4 Interpretational aspects of the rat

Until this point, we attempted to apply directly the axiomatics of QM to formulate the rat-in-the-box setup.

Now we would like to go through this process again, this time focusing on the interpretational aspects, i.e. we would like to go beyond borrowing a common understanding of the objects we deal with. Authors are aware of the fact that interpretation is a mathematically unprovable aspect of the theory, which changes *neither* the physical nature of modelled problem, nor the mathematics behind the model.

Nevertheless, this example aims towards understanding how QM describes the setup⁶ when both observer and a part of the system are consciousness and possess the free will⁷.

By the most used definition, an interpretation of QM is an attempt to explain how mathematical objects of QM correspond to the reality that can be experienced.

Objective facts:

1. State function $|\psi(t)\rangle$ is full description of the system which is rat-in-the-box in our case. This means that anyone knowing time evolution operator $\hat{U}(t)$ and $|\psi(t_{\text{fixed}})\rangle$ is able to compute $|\psi(t)\rangle$ for any $t \in \mathbf{R}$. This result is obtained in fully deterministic way by solving (14).
2. $|\psi(t)\rangle$ is mathematically represented by a finite-dimensional vector whose elements are complex numbers.
3. $|\psi(t)\rangle$ is *mathematically* a superposition (=linear combination) of a given basis in \mathcal{H} . Since $|\psi(t)\rangle$ depends on time t , either coefficients of superposition $c_j(t)$ are considered to be dependent on t or the basis itself is changing with time $\mathbb{B}(t) = \mathbb{M}(t)\mathbb{B}(0)$, where $\mathbb{M}(t)$ is unitary matrix expressing time basis evolution and $\mathbb{B}(0)$

⁶Here, setup means the experimental setup. For example, system+observer.

⁷Although observation process in QM works both for conscious and unconscious observer in the same way, we expect that deeper analysis of the living observer's perspective can help to narrow the gap between DM and QM.

is the matrix consisting of vectors forming basis in (4). From a mathematical point of view, both of those considerations are equivalent.

Interpretations considered:

1. $|\psi(t)\rangle$ is **expressing real nature of the system**. In our example, it is understood that rat is some “gas” that moves freely through the closed box and distributes over the rooms. In other words, at a fixed time moment the rat can occupy even several rooms partially at once. At the very moment when an observer opens the box, rat is found in a single particular room.

Idea in short: rat really *is* in a superposition state occupying several rooms at once, and she instantly “condenses” in a single room when measurement is performed.

Pros:

- ⊕ consistent with quantum understanding of micro physics (and Copenhagen interpretation of QM)
- ⊕ when accepted, no further interpretational problems arise

Cons:

- ⊖ seems unrealistic regarding any real-world rat (or any known macro object)
- ⊖ a free will of the rat (a part of the system) is hardly expressible/imaginable

2. **there’s no reality without observation**: the system is not real, only observed objects are. In other words: observed object/property exists only at the moment of the observation and due to it. In our example it means that the box is empty when it stays closed (there is *nothing* inside). Only at the moment when observer opens the box the rooms inside and the rat in one of them are formed and shown to the observer.

Pros:

- ⊕ accepts there is no (objective) reality when no observation is performed; implicitly it means reality can be anything when not observed
- ⊕ consistent with relational interpretation of QM [4]

Cons:

- ⊖ seems to be violated when 2 observers perform complementary observations on the same system
- ⊖ introduces very “crazy” image of the physical world which discards any hope of providing an explanation of how the nature works

3. **state vector is observer’s mental state regarding the system**: state function $|\psi(t)\rangle$ describes the state of the system relatively to the observer’s mind, i.e. $|\psi(t)\rangle$ does not express real physical properties, however it reflects them in some way. It expresses how observer sees (or can see) the system and possibly his expectations/ideas regarding the system. When observation is performed, it influences observer’s information about the system. We claim that:

- Influence of the observation process onto the system (or its part) is negligible in macro-scaled systems (like mentioned rat-in-the-box).
- Although there can be a direct causal link between the observation and discontinuous state change, it should be understood as the observer’s information gain, not physical changes in the system [2].

This interpretation is similar to the observation process as known from everyday life: a person does not influence TV by watching it, but he/she enriches his/her

knowledge by obtaining some information. We tend to understand the observation process in a similar way: the observer is obtaining some information and his mental state (regarding the system) is updated. In many macroscopic tasks the influence on the system due to observation is negligible (for instance watching TV, listening to lectures, measuring height/weight/distance/velocity/...).

Pros:

- ⊕ coincides with common human experience from macro world: gaining information
- ⊕ consistent with the basic concept of QBism [5]: observation is the experience that the observer gets from his action on the system

Cons:

- ⊖ unusual from the perspective of many physicists

5 Concluding remarks

The rat-in-the-box model presented in this paper serves as a simple example of how the formal postulates of quantum mechanics can be applied to describe a macroscopic, decision-oriented system. The formalism provides a coherent mathematical language for expressing uncertainty, state evolution, and observation in a unified way. While the present text focused on the theoretical formulation and interpretational aspects, preliminary numerical experiments have been carried out and will be presented separately. Future work will explore these computational results and extend the model toward more complex, data-driven and quantum-inspired representations of decision-making processes.

References

- [1] Dirac PAM. The Principles of Quantum Mechanics. 4th ed. Oxford University Press, USA; 1967. Available from: libgen.li/file.php?md5=2710c3ff396e7da678b4dc3e55f6121c.
- [2] Gaj A, Kárný M. Quantum Model of Uncertainty for Dynamic Decision Making [Master Thesis]; 2024. Czech Technical University. Master Thesis. Available from: <https://doi.org/10.5281/zenodo.15250012>.
- [3] Khrennikov AY. Open Quantum Systems in Biology, Cognitive and Social Sciences. Springer; 2023.
- [4] Rovelli C. Relational quantum mechanics. International Journal of Theoretical Physics. 1996 Aug;35(8):1637–1678. Available from: <http://dx.doi.org/10.1007/BF02302261>.
- [5] Fuchs CA. QBism, Where Next? 2023. Available from: <https://arxiv.org/abs/2303.01446>.

Acknowledgement

The authors acknowledge the contribution of the Grant Agency of the CTU in Prague, grant No. SGS25/167/OHK4/3T/14 and EU COST Action CA21169.

Fatigue limit of additively manufactured materials

Štěpán Hortlík¹, Ondřej Kovářík¹, Ján Kondás², Jiří Zýka³

¹Department of Materials, Faculty of Nuclear Sciences and Physical Engineering, Czech Technical University in Prague, Czechia

²Impact Innovations GmbH, Rattenkirchen, Germany

³UJP PRAHA a. s., Praha – Zbraslav, Czechia

Abstract

The Department of Materials at FNSPE, CTU in Prague, possesses unique equipment for fatigue crack growth rate testing, which has been already used for a broad range of materials. However, for a complete characterization of the fatigue process, it is necessary to design an additional experiment focused on the fatigue strength of specimens without macroscopic cracks. In this work, three new specimen geometries are proposed for this purpose, together with an analysis of methods for testing under stress amplitudes close to the fatigue limit. The proposed approach is experimentally verified in two case studies on materials produced by two different additive manufacturing techniques: cold spray (CSAM) and selective laser melting (SLM).

Introduction

At the Department of Materials FNSPE CTU, a well-established methodology exists for crack growth rate testing under cyclic loading. It provides reliable characterization of the crack propagation phase of fatigue damage [1]. To capture the entire fatigue process, however, an additional experimental approach is needed to characterize the phase of crack nucleation and growth of microscopic cracks. This means designing an experimental procedure and a sample geometry for fatigue strength investigation near the fatigue limit.

The common procedure for fatigue limit determination is the staircase method, which has been also standardized [2]. Its problem is that at least 15 specimens are required for each material and orientation (if anisotropy is anticipated). Furthermore, an initial guess and step size must be set before starting the testing trial [3]. These factors make this method very demanding for new, additively manufactured materials, as there is often only a limited number of specimens and the values of fatigue strength are completely unknown.

On the other hand, step-stress method [4] requires only around 5 specimens to do the same thing. Furthermore, the initial guess is not a critical parameter, and the tests can run parallelly in contrast to the staircase method. As the method consists of loading at a given number of cycles before an increase by the step size, the testing time for a single specimen is increased. However, this is not a significant issue when the frequency is high enough and the test itself requires no human assistance.

Materials and methods

Specimen geometry had to be developed to be suitable for bending fatigue testing, to fit in the existing resonance testing machine without much need for reconfiguration, and to have the possibility to be made entirely by EDM cutting. This is important to enable the fatigue characterization of additively made materials, which cannot be conventionally machined. Along with that, as much as possible from the existing standards for bending fatigue testing [5] is followed. This way, three different geometries are considered.

Hyperboloidal specimen was designed to be made by rotating an 10° inclined EDM wire around the main specimen axis. This was to be followed by cutting the clamping surfaces. Despite seeming straightforward at first, the cutting method is yet to be fully developed.

Thin wall hyperboloidal specimen is on the outside the same shape as hyperboloidal. The difference is a hole running through the whole specimen. This geometry is a custom design for fatigue testing of thin, SLM-made Inconel 718 grids to support UJP Praha a.s. project “Additive Manufacturing of Nuclear Fuel Components” (TAČR theta TS01020104). The complex geometry with only 0.3 mm thick wall in

the central part is made feasible by the fact that the specimens can be directly printed and tested without any further preparation.

Blunt notch specimen is a derivation from the standardized SE(B) specimen used for fracture properties testing [6]. Instead of making the notch sharp for crack initiation, a controlled radius of 1 mm was made to ensure acceptable geometrical accuracy. This is crucial, as the maximum stress in this specimen is strongly dependent on the notch depth and radius. Fatigue testing using this specimen was investigated in a case study of cold-sprayed Ti6Al4V made of two powder morphologies (crystalline, spherical) as sprayed and after heat treatment.

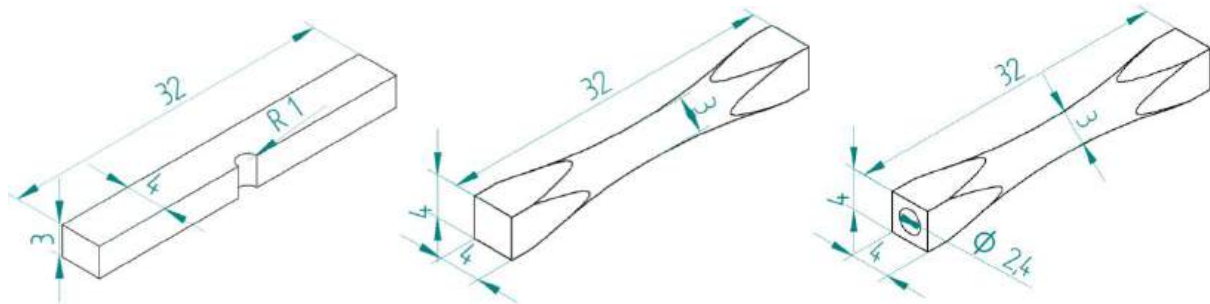


Figure 1: Specimen geometries investigated. Blunt notch specimen (left), hyperboloidal specimen (center) and hyperboloidal thin wall specimen (right)

For all the specimens considered, a FEM simulation was made to find out the maximum stress concentration ratio, which is in the range between 3 and 6. Furthermore, the stress gradient around the maximum is observed. That is important for explaining the discrepancy between the deviations achieved using different specimen geometries.

Results and discussion

Fatigue strength of CSAM Ti6Al4V is demonstrated in Fig. 2 (left). The high deviation observed for this group of materials is most likely caused by the specimen used as the maximum stress is found only in a small area at the tip of the notch. The crack initiation is therefore very susceptible to the local surface preparation and material non-homogeneity. Despite that, the results matched with uniaxial tests of identical materials [7], see Tab.1. Additionally, the fatigue limit was obtained from our bending data. The differences between as sprayed and heat-treated materials are most likely attributed to high porosity and insufficient particle bonding in as sprayed state, as confirmed by the porosity values and mechanical properties in Tab. 1.

	spherical as sprayed	crystalline as sprayed	spherical heat-treated blunt notch	crystalline heat-treated benchmark [7]
Porosity [%]	4,68 ± 0,30	4,63 ± 0,63	0,49 ± 0,30	0,48 ± 0,41
σ_a (MPa)	227 ± 18	228 ± 10	373 ± 36	412
$R_p0.2$ (MPa)	418	461	1008	940
σ_a/R_m	0.54	0.49	0.37	0.44

Table 1: Mechanical and fatigue properties of cold-sprayed Ti6Al4V.

The testing trial for SLM In718 is concluded in Fig. 2 (right). It involved step-stress tests, which indicated a clear fatigue limit above $5 \cdot 10^6$ cycles at 100 MPa. At higher load, standard constant amplitude tests were used. The results demonstrate well the merit of the proposed hyperboloidal geometry. The deviation from the Wöhler curve is minimal in the whole range of cycles. Additionally, an efficient testing strategy is demonstrated. Only 12 specimens are needed for accurate fatigue characterization of this material in a broad range between 10^3 and 10^7 cycles.

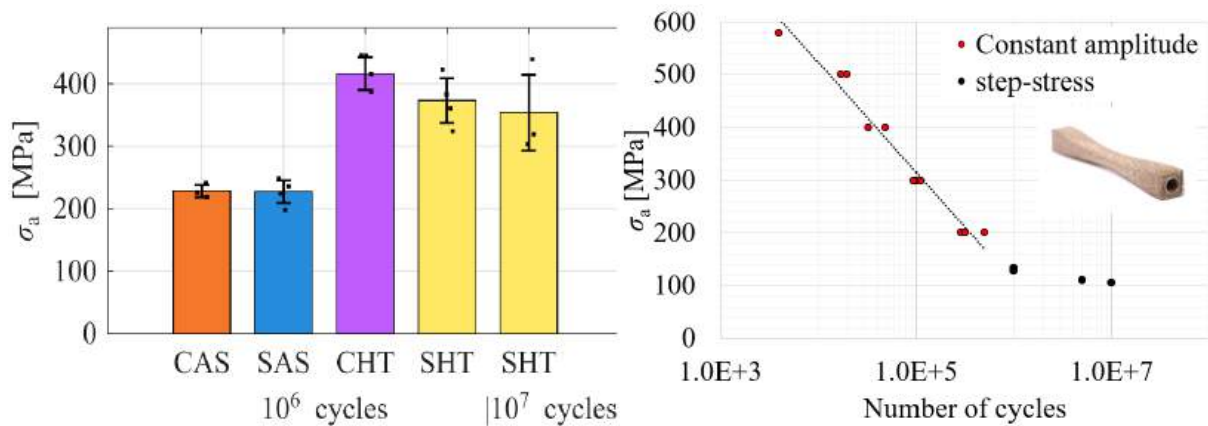


Figure 2: Fatigue strength results as the stress amplitude at $R = -1$ for CS Ti6Al4V (left) and for SLM In718 (right).

Conclusion

Step-stress method proved to be an efficient approach for determining the high cycle fatigue strength of additively manufactured materials with an unknown but assumed fatigue limit. Using this method, three specimen geometries were proved feasible for resonance bending testing at $R = -1$. This is suitable for fatigue strength measurement thanks to high frequency, automatic crack detection and inexpensive testing equipment.

The approach was tested in two case studies. The blunt notch specimen geometry caused significant data scatter for the set of four CSAM Ti6Al4V materials. However, it enabled fatigue testing of brittle, as-sprayed materials, which would not be measurable by conventional methods. SLM Inconel 718 was investigated using thin wall hyperboloidal specimen with great precision, finding the fatigue limit at 100 MPa.

References

- [1] O. Kovářík, P. Haušild, J. Čapek, J. Medřický, J. Siegl, R. Mušálek, Z. Pala, N. Curry and S. Björklund, "Resonance bending fatigue testing with simultaneous damping measurement and its application on layered coatings," *International Journal of Fatigue*, vol. 82, p. 300–309, 2016.
- [2] ISO, *ISO 12107:2012: Metallic materials–Fatigue testing–Statistical planning and analysis of data*, 2012.
- [3] C. Müller, M. Wächter, R. Masendorf and A. Esderts, "Accuracy of fatigue limits estimated by the staircase method using different evaluation techniques," *International Journal of Fatigue*, vol. 100, p. 296–307, July 2017.
- [4] R. Bellows, "Validation of the step test method for generating Haigh diagrams for Ti–6Al–4V," *International Journal of Fatigue*, vol. 21, p. 687–697, August 1999.
- [5] ISO, *ISO 1143:2021: Metallic materials — Rotating barbending fatigue testing*.
- [6] T. L. Anderson, *Fracture Mechanics*, CRC Press, 2017.
- [7] J. Kondas, "Private communication," 2025.

Atomic force microscopy

Michal Jůza

Department of Solid State Engineering, Faculty of Nuclear Sciences and Physical Engineering, Czech Technical University in Prague
juzamich@cvut.cz

Abstract

AFM is a versatile analytical tool that allows us to measure surface structure and properties of various samples with unprecedented resolution. Because of its unique abilities, AFM is nowadays being used in many applications including biology, physics, materials science, nanotechnology, medicine, chemistry and much more. AFM uses precise sharp tip to physically "feel" the sample instead of using interaction of electrons or photons like traditional microscopic techniques. With variety of available tips the device can be used to measure for example electrical charge or magnetic field with nanometre precision making 2D map of the measured properties.

Keywords: Atomic force microscopy, Scanning probe microscopy

Preface

The aim of this paper is to explain basic concepts of AFM, instruct how to measure with AFM and how to analyse obtained data. Information provided here mostly comes from the biography *Atomic force microscopy* from Peter Eaton and Paul West [1] as well as from the personal experience of the author.

Introduction

Atomic force microscopy is an amazing technique that allows us to see and measure surface structure with unprecedented resolution and accuracy. Using AFM it is possible to see the arrangement of individual atoms in a sample or to see the structure of individual molecules. AFM was developed in 1986 by G. Binnig, C. F. Quate, Ch. Gerber as an evolution of Scanning tunneling microscope (STM). Using STM it was possible to achieve extraordinary resolution, but it was limited only to conductive samples and the measurement needed to be carried out under high vacuum. Using AFM, however, it is possible to examine various samples with little to no treatment and to measure in atmospheric conditions and even in liquid. These benefits caused revolution in biology, because it was then possible to analyse biological samples, cells or molecules in their native environment for the first time with unmatched precision. The principles of AFM are different to "traditional" microscopic techniques like electron or optical microscope, which all relies on interaction of some particles (electrons, photons, etc.) with the specimen. Contrary to that the AFM works by physically scanning the sample with sharp tip and using the feedback system measuring the height (or other properties) of the sample pixel by pixel and thus forming 2D map of the measured properties.

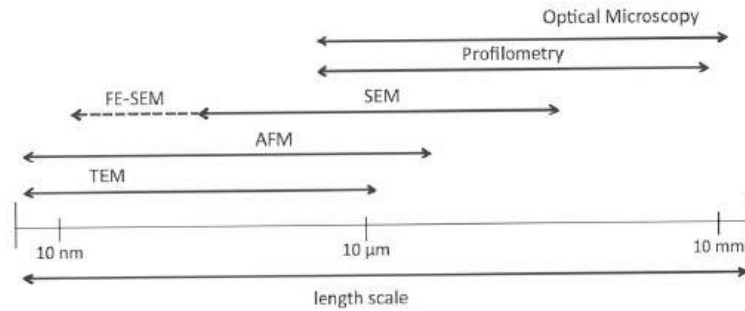


Figure 1: Comparison of length scales of various microscopic techniques.

Instrumentation

The AFM instrument consists of several key components. One of the challenges is precise tip-sample movement, which is necessary to obtain high-quality data. This is achieved by combining piezoelectric and stepper motors. The AFM instruments can be divided into probe-scanning and sample-scanning (Figure 2). The advantage of a probe scanning AFM is that it can scan larger samples. The stepper motors represent the coarse motion needed to approach to the desired feature of the sample. The piezoelectric actuators are used for precise scanning with sub-nanometre precision. The actual scanning speed is limited by the resonance frequency of the piezoelectric elements, which often suffer from some kind of non-linear behaviour and may suffer from hysteresis or creep. The mentioned problems need to be compensated during the measurement or addressed later during the image processing. The actual force sensor in most AFM instruments uses the so-called optical lever (see Figure 3). The laser beam is aimed at the end of the cantilever and by bending or movement of the cantilever the position of the reflected beam on the detector changes. This change in intensity of the light in the different quadrants is then used to define the force applied to the probe. The optical lever method is very sensitive to subtle movements of the cantilever but for it to function properly the precision alignment is necessary.

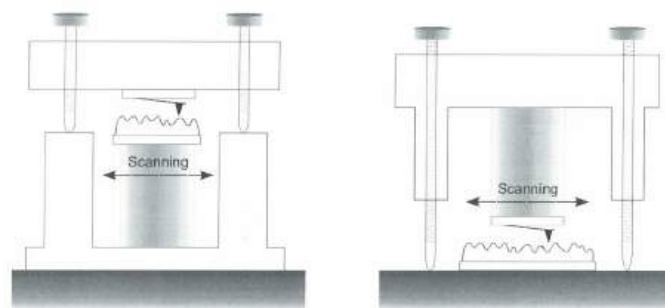


Figure 2: The difference between sample-scanning (left) and probe-scanning (right) AFM. In a sample scanning AFM the sample is mounted on piezoelectric actuators and the probe remains fixed. In probe scanning AFM the sample remains fixed and the probe is scanned.

Another key component is the control electronics and the feedback system. The electronics generates the scanning signals for x - y positioning of the scanner. The feedback

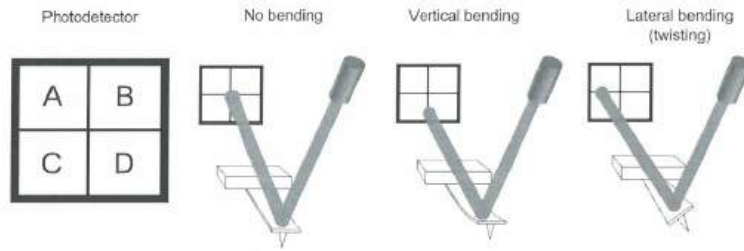


Figure 3: Schematic diagram of the optical lever.

control based on input from force sensor ensures the height of the probe above the surface is kept constant (in the constant force mode) by changing the z coordinates of the probe to match the surface topology. Another possible mode is the constant height mode, where the z coordinate of the probe is kept constant and the force is recorded. Note that the constant height mode can be used only with very smooth samples or at smaller horizontal ranges, where the height change is not so significant. The feedback loop is based on the PID regulator (usually only PI regulator) with P,I (and D) parameters subject to tuning. The control electronics needs to be fast yet precise and with low noise floor. The control electronics is responsible for controlling the coarse movement using the stepper motors. In the case of the oscillating modes (see below) the control electronics also drive the oscillating probe around its resonance frequency and measures its amplitude and phase. At last, the control electronics acquires the measured data and saves them for the further analysis.

Modes of measurement

The basis of AFM microscopic technique is the measurement of the topography of the sample. In these topography modes the height profile of the sample is measured using the feedback loop, discussed above. However, contrary to "classical" microscopes (e.g. optical or electron microscopes), the outcome of described measurement is not a conventional image, but rather a 2D map of height coordinates. The topography modes can be divided into contact mode and oscillating modes. Contact mode was the first and most basic mode developed for AFM. In contact mode the probe tip is close enough to the surface of the sample so that their mutual force interaction is in the repulsive regime. This has several implications. Firstly, the tip-sample force might be considerable and may damage the probe or the sample and the surface can be affected by the tip. However, the contact mode has the greatest resolution compared to the oscillating modes and also features highest scanning speed.

Oscillating modes, which were described in the first paper on AFM in 1986, are divided into non-contact mode and intermittent-contact mode. Contrary to the contact mode, the non-contact mode operates exclusively in the attractive interaction regime. When the distance between the probe and the surface changes, the amplitude and the phase changes, which is used by the feedback loop to adjust the height of the probe above the sample. The non-contact mode has benefit of reduced tip-sample forces and therefore reduced risk of damage of the sample or probe wear compared to the contact mode. Nevertheless, the theoretical resolution of the non-contact modes is also reduced.

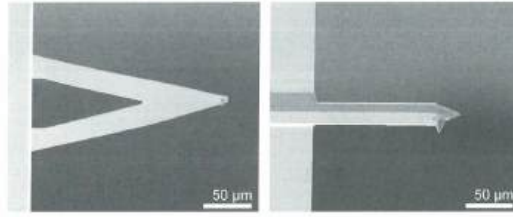


Figure 4: Example of contact mode probe (left) and oscillating modes probe (right). The probe for oscillating modes is usually much stiffer and more prone to breaking than the contact probe.

The intermittent-contact mode operates in both attractive and repulsive regime with much greater amplitude of probe oscillations than the non-contact mode. Because of the larger amplitude the intermittent-contact mode has higher possibility of braking the probe tip than non-contact mode, but still lower than contact mode. However, the intermittent contact mode is advantageous for measuring samples in liquid layer, because the oscillating force withdraws the tip from the contamination layer on the surface in each oscillation, reducing the effect of capillary forces between the tip and sample in comparison to non-contact mode.

In addition to topographic modes there also exist a variety of non-topographic modes. One of them is the force spectroscopy. It uses the force sensing capabilities of an AFM to obtain force-distance curves of the sample among its surface point-by-point. Also the sharp and hard tip can be used for nanoindentation. In this mode the tip is pressed into a sample and the load-displacement curves are measured. The size of indents can be then measured by optical microscope. Another non-topographic mode is lateral force microscopy. The lateral forces are measured based on the bending of cantilever. Magnetic force microscopy and Electric force microscopy uses special probes to obtain data about electric field and magnetic field. Using Scanning Kelvin probe microscopy the work function of the surface can be observed at atomic or molecular level. Scanning thermal microscopy is used to create map of thermal conductivity and thermal capacity. It is worth mentioning that the AFM can be used not only for measuring sample surface properties but also to manipulate or modify them. AFM-based lithography is one of the examples of surface modification method using AFM instrument.

Measurement

One of the biggest advantages of AFM is the requirement of little to no sample preparation. It is not necessary for the sample to be electrically conductive (like in the case of STM) and the measurement can take place in various environments and temperature ranges. The only major requirement is the proper fixation of the sample to the substrate in the AFM instrument, which is especially crucial for biological samples and nanoparticles. It is beneficial for the sample to be clean and contamination-free for best results possible. Namely for the oscillating modes it is also recommended to minimize the electromagnetic and acoustic noise in the vicinity of the apparatus. Particulate samples, polymers, DNA molecules, cell structures, bacteria or nanotubes are among the examples of specific samples that needs additional preparation. In contact mode the precise alignment of the

optical lever (if present) is crucial and in oscillating modes the resonance frequency tuning is necessary. All modes require further feedback loop tuning for best results.

The key part of the measurement is the approach of the probe to the surface of the specimen. At first, the operator needs to find the feature of interest using the stepper motors usually with the aid of optical microscope to observe the actual position of the probe. Then he may perform the coarse approach using optical inspection. Final stage is the semiautomatic or automatic probe approach process. In this process the piezoelectric element moves sample toward the probe or the probe toward the sample until the maximum extension is reached. Then the piezoelectric element retracts and the stepper motors approaches the corresponding amount and the cycle repeats until the surface is reached.

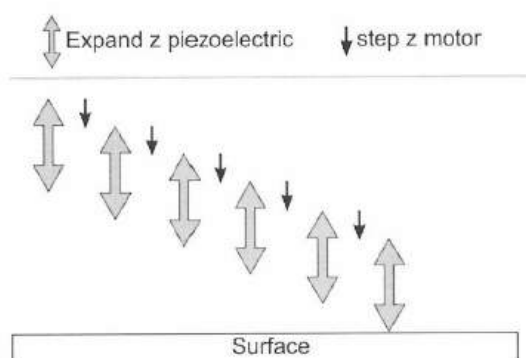


Figure 5: Woodpeckers' probe approach technique. The surface is approached by alternatively expanding the piezoelectric element, and the z stepper motor. As soon as the surface is reached, the feedback system gets activated.

Image processing and image artefacts

The important part of the AFM measurement is the image processing. Because the AFM dataset contains much more data than typical image, which has 256 shades of gray (8 bit), whereas the vertical resolution of typical Atomic force microscope is 65536 steps (16 bit). That is why to obtain all the useful data of the dataset the proper processing must be made. One of the basic image processing step is levelling, e.g. polynomial fitting (see Figure 6) or plane levelling.

One of the drawbacks of AFM is the possibility of image artefacts. These artefacts results from damaged or blunt probe. Broken cantilever prevents measurement at all. It needs to be expressed, that final image is convolution of the probe shape and topology of the sample, so blunt probe does not allow to see small features. (See Figure 7). Another artefact can be caused when the probe has more than one tip. This defect can cause "ghost" features in regular pattern over the measurement, which should be exposed by the operator. Bad parameters tuning can cause artefact as well: with feedback set too high, noise can appear in the record, whereas when the feedback is set to low, smaller features might be missed at all. Another group of image artefacts are the ones caused by incorrect processing. These includes bad fitting or inappropriate data modification. These artefacts can hide real features and induce false ones.

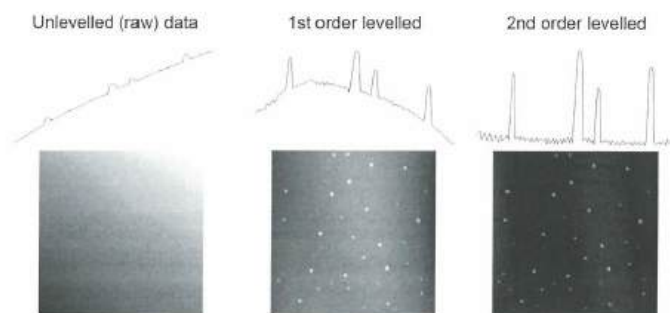


Figure 6: Illustration of the effect of first and second order polynomial line levelling.

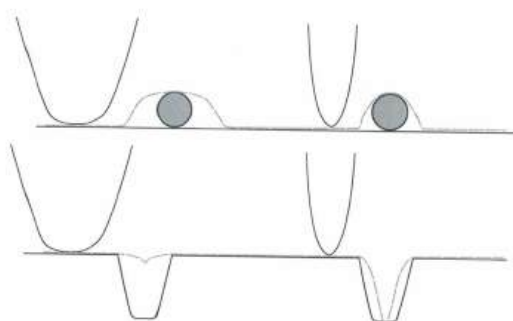


Figure 7: Illustration of probe-based artefacts. Convex features such as particles tend to appear wider with blunt probe, although feature height might be accurate, whereas concave features as holes tend to appear smaller and shallower with blunt probe.

Conclusion

AFM is well established and useful analytical tool that can be used in many different areas. The application of AFM span over multiple science, medical or engineering fields. Among some examples are material science, chemistry, biology, physics, nanotechnology, astronomy or medicine. The availability and accessibility of the AFM nowadays makes it perfect tool for students to expand and practice their technical and scientific abilities.

References

- [1] P. Eaton, P. West. *Atomic force microscopy*. Oxford University Press, 2010. ISBN 9780199570454.

Acknowledgment

This work was supported by the Grant Agency of the Czech Technical University in Prague, grant No. SGS25/168/OHK4/3T/14

Gas pressure optimization of titanium nitride thin films deposition by IJD method

Bc. Martin Kolář, Ing. Jakub Skočdopole Ph.D.

Department of Solid State Engineering, Faculty of Nuclear Sciences and Physical Engineering, Czech Technical University in Prague

Abstract

Titanium nitride is often used as a protective coating due to its hardness. This material is mostly deposited by pulsed laser deposition or magnetron sputtering. Ionized jet deposition has a potential to improve and diversify ways of making titanium nitride thin films. We manufactured 2 set of films using different deposition pressures. One set was prepared with nitrogen other with mixture of nitrogen and hydrogen. We analysed the samples to find out how layer characteristics change with gas pressure. Based on the XRD and raman data, neither higher or lower gas pressure is preferable for nitridation. In contrast, lower gas pressure contributes to higher film growth, based on AFM data. Data indicate only small difference between these two sets.

Keywords: IJD, TiN, thin films

Introduction

TiN is very tough ceramic material with interesting opto-electronic properties. It is widely used as a protective layer for tool ranging from drills to medical devices. [1, 2]

IJD is relatively new deposition method, which uses electron pulses to ablate material creating plasma. This plasma then precipitate on substrate and form thin film. [3]

Aim of this research is to investigate deposition of TiN using IJD as its high ionization of gas during deposition[3] could be beneficial for TiN nitridation. We crated 2 sets of thin layers, one using nitrogen and other using mixture of nitrogen and hydrogen. Samples in the sets differ by pressure of deposition gas.

Materials and Methods

As a substrates we used laboratory glass, silicon wafer and AISI304 steel sheet. We washed them with purified water, isopropyl alcohol and acetone and in ultrasonic bath in acetone. Thin films were deposited from titanium target using IJD JetDep100 deposition system in Applied photonics and quantum technologies laboratory of Department of Solid State Engineering Faculty of Nuclear Sciences and Physical Engineering, Czech Technical University in Prague. IJD source supplied 17 kV of voltage and the frequency of pulses was 100 Hz. Pure titanium was used as a target. Deposition lasted 30 minutes, apart from sample TiN-5, which deposition lasted only 15 minutes due to high degradation of the target. Due to low gas pressure and degradation of the target during deposition of samples TiN-4, TiN-5 and TiNH-4 the frequency of pulses was not stable. First set was created with nitrogen as a deposition gas and second set was created in mixture of nitrogen

(90%) and hydrogen (10%). Samples in sets differed in pressure of deposition gas as shown in tables 1 and 2.

Table 1: Nitrogen pressure of the first set

Sample	TiN-1	TiN-2	TiN-3	TiN-4	TiN-5
Gas pressure [bar]	8,0	7,0	6,0	5,0	4,5
Pressure in chamber [10^{-4} mbar]	3,3	3,5	3,0	2,9	2,0

Table 2: Pressure of nitrogen and hydrogen mixture of the second set

Sample	TiNH-1	TiNH-2	TiNH-3	TiNH-4
Gas pressure [bar]	7,0	6,0	5,0	4,5
Pressure in chamber [10^{-4} mbar]	3,4	2,6	2,2	2,2

We have determined the thickness of layers by AFM measurement of layer-substrate interface and subsequent analysis in Gwyddion program. We have analysed chemical and phase composition by XRD and Raman spectroscopy methods.

Results

We prepared nine samples of titanium nitride thin films. Samples TiN-1, TiN-2, TiN-4, TiN-5, TiNH-2 a TiNH-4 had cracks on their surface. TiN-1 stated cracking after being withdrawn from the vacuum chamber.

AFM

The width of the layers as determined by AFM are in range 142-1007 nm as shown in tables 3 and 4.

Table 3: Thin layer thickness of the first set

sample	TiN-1	TiN-2	TiN-3	TiN-4	TiN-5
Gas pressure [bar]	8	7	6	5	4,5
Thickness [nm]	285±2	142±2	948±10	300±27	537±10

Table 4: Thin layer thickness of the second set

sample	TiNH-1	TiNH-2	TiNH-3	TiNH-4
Gas pressure [bar]	7	6	5	4,5
Thickness [nm]	220±6	154±2	1007±8	500±8

XRD

Qualitative phase analysis revealed presence of titanium nitride and titanium oxide in all samples. Samples TiN-3, TiN-4, TiN-5, TiNH-3 and TiN-4 also contain hexagonal titan.

Raman spectroscopy

Almost every Raman spectra of samples contained broad peak around 200 cm^{-1} and less intensive around 400 cm^{-1} and 550 cm^{-1} as shown in figure 1 of sample TiN-1.

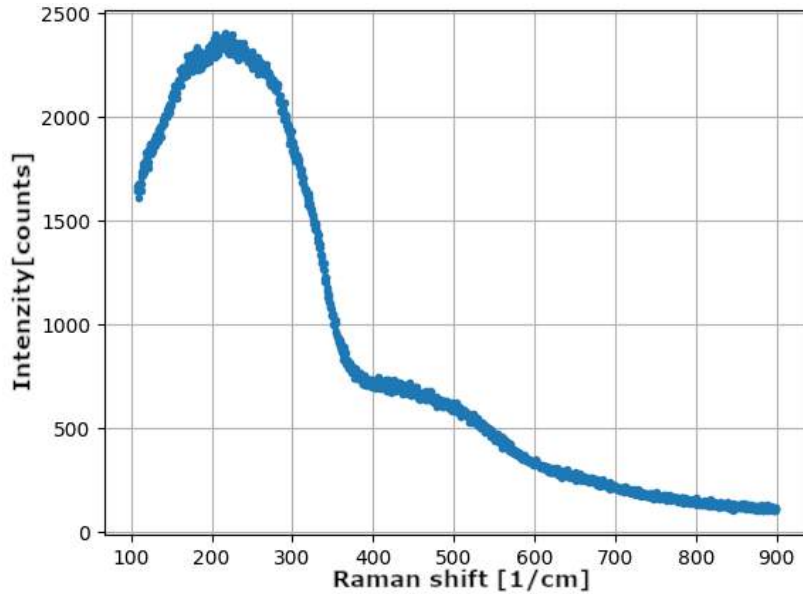


Figure 1: Raman spektra of sample TiN-1

Only exception was Raman spectra of sample TiN-3 with maxima around 200 cm^{-1} , 320 cm^{-1} and 550 cm^{-1} as shown in figure 2.

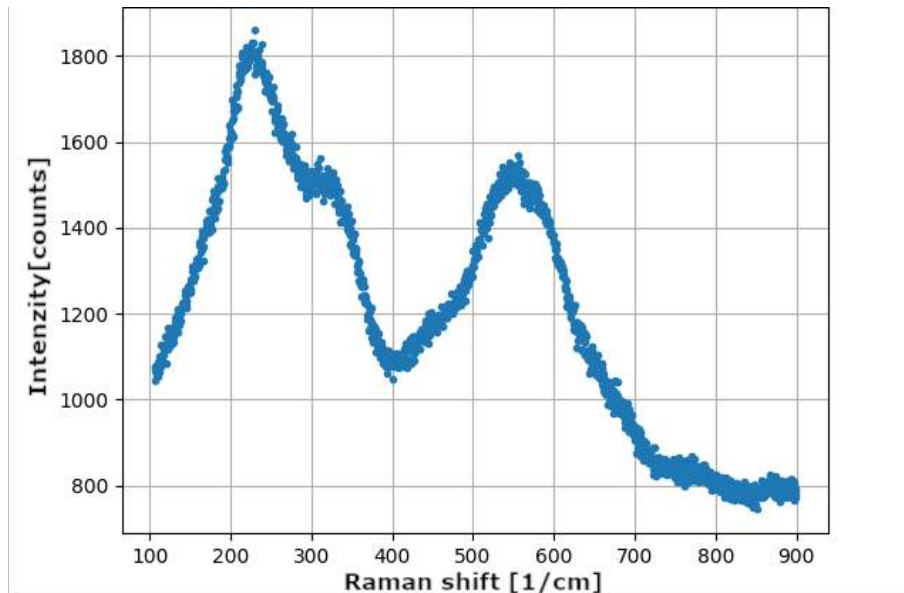


Figure 2: Raman spektra of sample TiN-3

Discussion

After calculating deposition growth of the layers from sample thicknesses measured by AFM, we see that there is an exponential dependency of deposition growth rate on gas pressure of samples with stable frequency during deposition, as shown in figures 3 and 4. By lowering gas pressure the deposition growth rate increases. The tendency of both sets have the same character only shifted. First set have the same growth rate on with higher gas pressure.

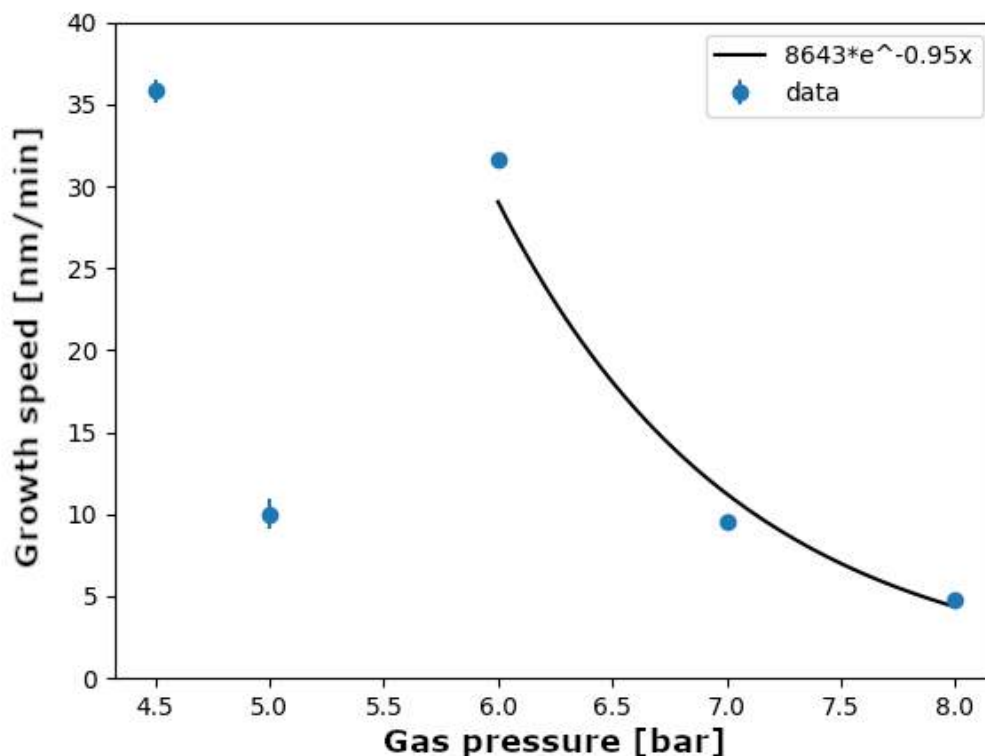


Figure 3: Growth rate of the first set in relation to gas pressure

XRD analysis discovered presence of TiN and TiO in the samples. Hexagonal titan was found in samples TiN-3, TiN-4, TiN-5, TiNH-3 and TiN-4. Those samples were deposited with lower gas pressure, therefore the nitridation could be lower with lower gas pressure.

Highest peak around 200 cm^{-1} on Raman spectra of almost all samples is combination of signal from nitrogen vacancies and from titanium oxonitride [4]. Those signals also contribute to peak between 400 cm^{-1} and 500 cm^{-1} , which could also originate from titanium oxide [4]. Peaks around 220 cm^{-1} and 320 cm^{-1} on Raman spectra of sample TiN-3 originate from nitrogen vacancies and peak around 550 cm^{-1} originate from titanium vacancies. Sample TiN-3 has the highest nitridation of all samples. This with combination of finding of hexagonal titan with XRD on samples deposited with low gas pressure could mean that with low gas pressure the titan is not sufficiently quickly ionized and with high gas pressure the ionization of nitrogen is not sufficient. Medium pressure is therefore ideal for nitridation.

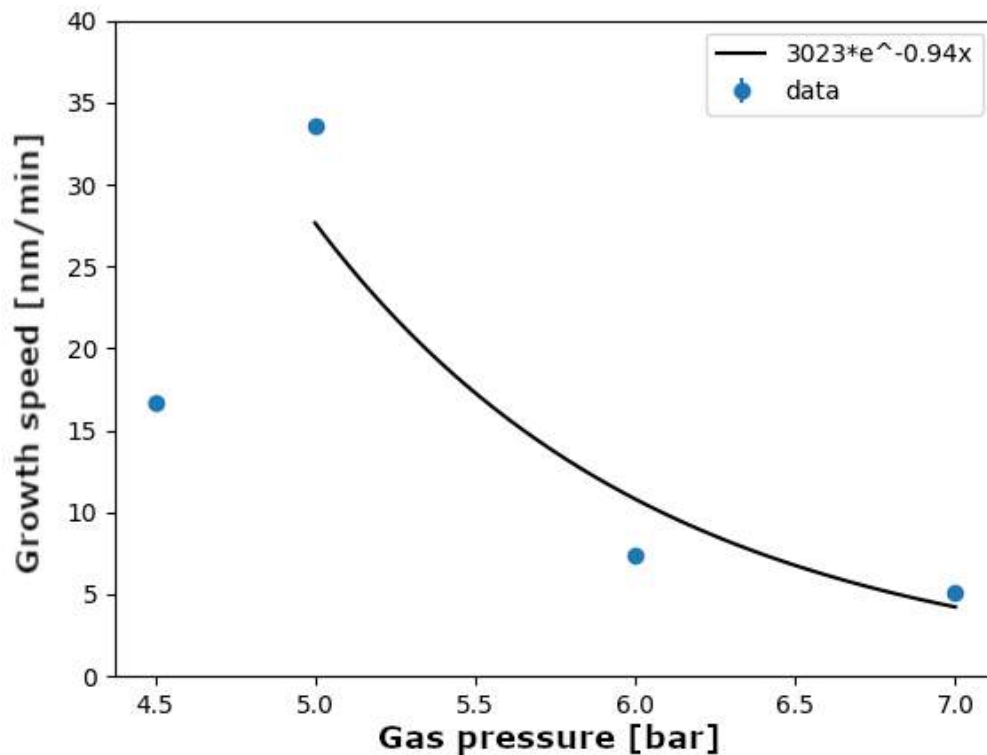


Figure 4: Growth rate of the second set in relation to gas pressure

Conclusion

Totally nine samples in 2 sets were created. All samples contain titanium nitride and oxide and all samples except TiN-3 have lower concentration of nitrogen than titan. AFM analysis revealed exponential dependency of growth rate on gas pressure. Raman and XRD analysis discovered 2 opposite trends in dependency of nitridation on gas pressure leaving medium gas pressure best for nitridation.

Acknowledgement

This work was supported by the Grant Agency of the Czech Technical University in Prague, grant No. SGS25/168/OHK4/3T/14

Detekce laserového poškození pomocí odraženého He-Ne laserového záření

František Novák^{1,2}, Liliia Uvarova¹, Mihai-George Mureşan¹, Šárka Němcová^{1,3}

¹Centrum HiLASE, Fyzikální ústav AV ČR

²Katedra laserové fyziky a fotoniky, Fakulta jaderná a fyzikálně inženýrská, České vysoké učení technické

³Ústav přístrojové a řídicí techniky, Fakulta strojní, České vysoké učení technické
novakfr3@fjfi.cvut.cz

Abstrakt

Pro využití laserových systémů ve vesmíru je třeba zjistit prahovou hustotu energie laserem indukovaného poškození jejich optických prvků ve vakuu. Standardní *in-situ* detekce poškození je v prostředí vakua problematická. V této práci je představen systém pro *in-situ* detekci poškození pomocí od vzorku odraženého He-Ne laserového záření. Systém umožňuje získat přesný obraz vzniklého poškození a sledovat jeho okolí. Díky čtyřnásobnému zvětšení lze úspěšně detekovat poškození o rozměrech od 35 μm .

Klíčová slova: : *In-situ* detekce poškození; práh laserem indukovaného poškození; He-Ne laser, LIDT.

Úvod

Prahová hodnota hustoty energie či intenzity laserového záření, která indukuje poškození, představuje důležitou charakteristiku každé optické komponenty v laserovém systému. Zejména rozvoj vysokovýkonových laserových systémů (např. [1–3]) klade vysoké nároky na odolnost používané optiky vůči laserovému poškození. Vzhledem k rozšířenému užívání optiky s vysoce odrazivými či antireflexními vrstvami, patří zvyšování odolnosti mezi dlouhodobé cíle výzkumu technologií naprašování dielektrických vrstev [4].

Určování prahu poškození (dále LIDT z anglického *Laser-Induced Damage Threshold*) je procedura s postupem detailně popsáním ISO normou 21254. Aparatura pro jeho měření se skládá z laseru, variabilního atenuátoru, systému pro vedení svazku, systému pro zaostřování svazku, držáku vzorku a zařízení pro *in-situ* detekci poškození. *In-situ* detekci poškození je možné realizovat více způsoby, z nichž k nejběžnějším patří: pozorování vzorku pomocí rychlé kamery [5], pozorování vzorku pomocí mikroskopu s dlouhou pracovní vzdáleností [6], detekce indukovaného fluorescenčního záření [7] a detekce rozptýleného záření [8, 9].

V případě laserových systémů s potenciálním využitím ve vesmíru je třeba při testování LIDT zohlednit vlivy vesmírného prostředí. Mezi nejmarkatnější patří vakuum, dále pak extrémní teploty, kontaminace, bombardování ionty atd. [10]. Zahnutí vakua vyžaduje testování vzorku ve vakuové komoře. Při takovém testování je zapotřebí omezit možné zdroje kontaminace ve vakuové komoře - tj. kromě vzorku v držáku se v komoře nesmí nacházet žádné jiné optické komponenty. To má za následek komplikace při zavádění standardních metod *in-situ* detekce poškození.

Jedna z možností přístupu k *in-situ* detekci poškození při testování LIDT vzorku ve vakuu je využití He-Ne laseru - viz např. [8, 9, 11, 12]. Existují dva hlavní principy, na kterých je technologie detekce pomocí He-Ne laseru postavena. Prvním z nich je detekce rozptýleného záření He-Ne laseru, které probíhá na poškození. Tento princip byl využit u prací [8, 9]. V práci [8] bylo dosaženo rozlišení menší než $1 \mu\text{m}$, pomocí kontinuálního He-Ne laseru. V tomto systému je nicméně umístěn objektiv s desetinásobným zvětšením přímo ve vakuové komoře, což je z hlediska čistoty prostředí nevhodné. Detekční systém na principu rozptýleného He-Ne laserového záření je uveden též v práci [9], ve které se ve vakuové komoře mimo držáku se vzorkem nic nevyskytuje. Autorem uvedené rozlišení je přibližně $5 \mu\text{m}$. Systém využívá periodicky přerušovaného He-Ne laseru, díky čemuž lze lépe filtrovat nežádoucí šum od slabého signálu rozptýleného záření (*lock-in amplifier* [13]).

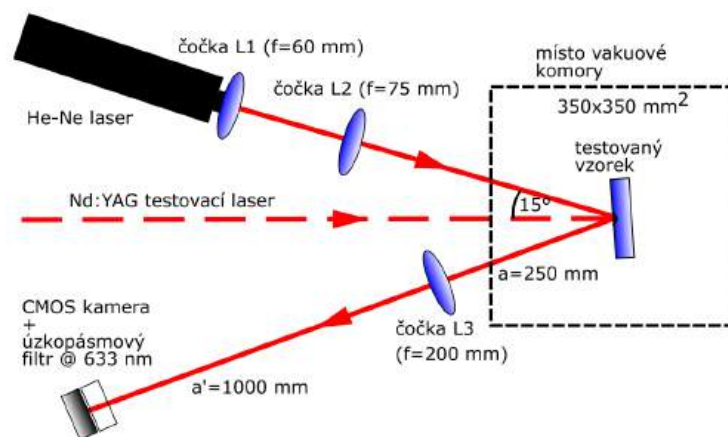
Druhým z principů je detekce na základě změny intenzity prošlého či odraženého He-Ne záření - viz např. [11, 12]. Ke změně intenzity dochází kvůli rozptýlení či difúznímu odrazu fotonů na vzniklém poškození. V práci [11] je poškození detekováno jako změna měřeného výkonu od testovaného vzorku odraženého kolimovaného He-Ne laserového svazku. V práci [12] je He-Ne laserový svazek kolineárně přiveden na vzorek. Vzorkem prochází a zobrazuje ho 3x zvětšený na CMOS kameře. Bohužel zde není uvedeno rozlišení systému.

V této práci je detailně popsán a charakterizován systém pro *in-situ detekci* poškození na základě zobrazení vzorku se čtyřnásobným zvětšením pomocí odraženého He-Ne laserového záření bez umístění optiky detekčního systému do vakuové komory. Detekční systém bude používán v LIDT stanici v centru HiLASE Fyzikálního ústavu AV ČR.

Experimentální uspořádání

V LIDT stanici umístěné v centru HiLASE, které je součástí Fyzikálního ústavu AV ČR, se pro vytváření poškození používá Nd:YAG laser (Q-smart 450, Lumibird) s centrální vlnovou délkou 1064 nm . Nd:YAG laser pracuje v pulzním režimu, jehož je dosaženo metodou Q-spínání. Délka impulzu činí $8,5 \text{ ns}$ a laser je schopen dosáhnout energie v impulzu až $0,5 \text{ J}$. Velikost energie v impulzu laserového svazku lze měnit pomocí atenuátoru, který je tvořený $\lambda/2$ vlnovou destičkou a polarizační kostkou. Pro účely tohoto měření byl laser zaostrěn na vzorek pomocí čočky o ohniskové vzdálenosti 500 mm . Úhel dopadu laserového svazku na vzorek byl 3° - častá hodnota úhlu dopadu, pod kterou je optika testovaná (pokud je pracovní úhel dopadu optické komponenty 0° , volí se 3° k zamezení přímému odrazu testovacího záření zpět do laseru). Laserový svazek na vzorku měl průměr ($1/e^2$) $169 \mu\text{m}$ a dosahoval elipticity 98% .

Schéma užitého laserového systému pro detekci poškození je zobrazeno na obrázku 1. Jádrem systému tvořil lineárně polarizovaný He-Ne laser (HNLO50L, Thorlabs) o vlnové délce $632,8 \text{ nm}$. Hodnota průměru svazku ($1/e^2$) na výstupu byla $0,81 \text{ mm}$. He-Ne laser byl nastaven tak, aby jeho osa svazku svírala s osou svazku laseru Nd:YAG 15° . Svazek následně procházel plano-konvexními čočkami L1 o ohniskové vzdálenosti 60 mm a L2 o ohniskové vzdálenosti 75 mm . Čočka L1 byla umístěna hned na výstupu laseru. Laserový svazek dopadal na vzorek umístěný v držáku pod úhlem 18° (3° natočení vzorku vůči Nd:YAG laseru a 15° vůči ose svazku Nd:YAG laseru) a jeho dopadová plocha svazku překrývala dopadovou plochu svazku Nd:YAG laseru. Laděním vzdálenosti čoček L1 a L2 mezi sebou navzájem bylo možné měnit hodnotu průměru svazku He-Ne laseru na vzorku. V případě této práce byla velikost svazku nastavena na 11 mm .



Obrázek 1: Schéma systému pro *in-situ* detekci poškození pomocí odraženého He-Ne laserového záření. L1, L2 – osvětlovací čočky, L3 – zobrazovací čočka s ohniskovou vzdáleností $f=200$ mm, a – předmětová vzdálenost, a' – obrazová vzdálenost.

Pro účely testu systému pro detekci byl zvolen křemíkový wafer $43 \times 43 \text{ mm}^2$ o tloušťce $0,525 \text{ mm}$ s leštěnou jednou stranou. Index lomu křemíku činí pro vlnovou délku $632,8 \text{ nm}$ $3,88$ [14], což pro úhel dopadu 18° znamená reflektanci 36% . Neodražené záření je buď absorbováno nebo rozptýleno. Vzorek byl umístěn v mechanickém držáku, jež byl připevněn ke dvěma motorizovaným lineárním posuvům, které vzorkem pohybuji kolmo dopadajícímu Nd:YAG laserovému svazku.

Po odrazu procházel svazek zobrazovací čočkou L3 a dopadal na CMOS kameru (Beamage-3.0, Gentec) s čipem 2048×1088 pixelů o rozměrech $11,3 \times 6,0 \text{ mm}^2$ a s rozměry pixelu $5,5 \times 5,5 \mu\text{m}^2$. Před kamerou byl umístěn úzkopásmový filtr pro $632,8 \text{ nm}$ pro odstínění nežádoucího signálu okolí. Vzdálenost mezi vzorkem a zobrazovací čočkou L3 a , její ohnisková vzdálenost a vzdálenost mezi čočkou L3 a kamerou a' byly nastaveny tak, aby bylo dosaženo maximálního zvětšení obrazu vzorku. To mělo vést ke snížení limitu velikosti nejmenšího detekovatelného poškození (velikost pixelů na kamerě). Dle zákonů geometrické optiky bylo dosaženo zvětšení $Z=4$ nastavením vzdáleností $a=250 \text{ mm}$, $a'=1000 \text{ mm}$ a zvolením čočky L3 s ohniskovou vzdáleností 200 mm . Vyšší hodnoty zvětšení nemohlo být dosaženo kvůli zachování prázdné vakuové komory a celkové kompaktnosti systému (součet vzdáleností $a'+a$ by neměl přesáhnout vzdálenost mezi He-Ne laserem a vzorkem, tj. asi 1300 mm). Na základě hodnoty zvětšení a rozměrů pixelu byl stanoven teoretický limit velikosti detekovatelného poškození na $7 \mu\text{m}$.

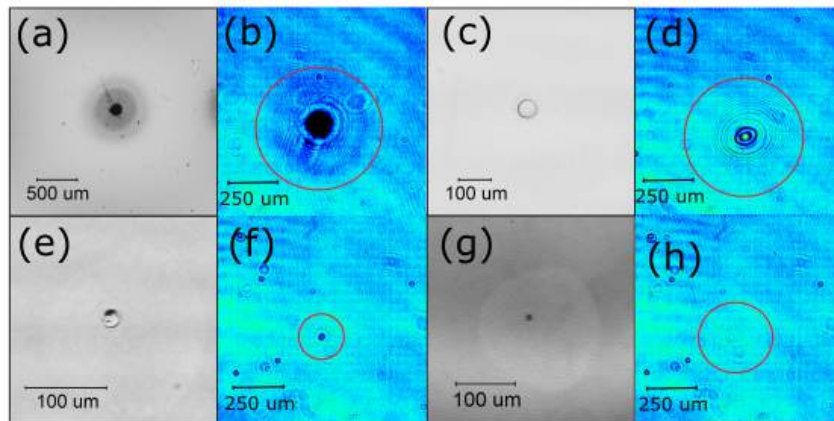
Výsledky a diskuse

Pomocí Nd:YAG laseru byla do křemíkového waferu vytvořena série 22 od sebe ekvidistantně vzdálených poškození. Ve snaze získat různé rozměry poškození byla měněna hustota energie laseru a počet impulzů dopadající na jedno místo. Série 22 vytvořených poškození spolu s 4 poškozeními z předešlých experimentů se pohybovala v rozsahu velikosti průměru od $10 \mu\text{m}$ do $210 \mu\text{m}$. Struktura a velikost poškození byly analyzovány pomocí konfokálního mikroskopu (OLS5000, Olympus). Systém detekce poškození byl testován *in-situ* po vytvoření série poškození, tj. ne v reálném čase. Vyjma nejmenšího

Tabulka 1: Seznam důležitých míst zkoumaných během experimentů s detekcí He-Ne laserem a jejich parametrů na vzorku křemíkového waferu. Místa 10 a 21 byla nově poškozena, zatímco místa 25 a 26 byla poškozena již dříve. Rozměry poškození byly označeny jako Δx a Δy .

#	Hustota energie (J/cm ²)	Počet impulzů	Δx (μm)	Δy (μm)	He-Ne Detekce
10	3.6	300	165	155	ano
21	3.0	250	60	55	ano
25	–	–	35	30	ano
26	–	–	5	10	ne

poškození o velikosti $5 \times 10 \mu\text{m}^2$ byla všechna poškození systémem detekována, tj. pozorovatel mohl poškození dobře identifikovat na obrazu z CMOS kamery. Nejmenší detekované poškození mělo rozměry $35 \times 30 \mu\text{m}^2$. Charakteristika nejdůležitějších poškození je uvedena v tabulce 1. V tabulce je uvedeno větší poškození (v pořadí 10. vytvořené), nejmenší indukované poškození (v pořadí 21. vytvořené), nejmenší detekované poškození (v pořadí 25.) a nejmenší poškození v celém měření (v pořadí 26.). Srovnání obrazu poškození z konfokálního mikroskopu s obrazem na CMOS kameře je pro nejdůležitější poškození na obrázku 2. U většího poškození (10) a nejmenšího vytvořeného poškození (21) lze na obrázcích na CMOS kameře poměrně slušně pozorovat morfologii poškození - toto je obecně jedna z výhod oproti detekci na základě rozptylu světla. Na druhou stranu u nejmenšího detekovaného poškození (25) může být poškození poměrně snadno zaměnitelné s obrazy od znečištění na optice. Záměnu lze vyloučit v případě in-situ detekce v reálném čase testu pořízením obrázku před a po vystavení vzorku laserovému záření a jejich následnému srovnání. V případě in-situ detekce, která nebyla provedena v reálném čase (toto měření), byla záměna vyloučena jednak na základě ekvidistantní vzdálenosti poškození, jednak pohybem vzorku pomocí motorizovaného posuvu. Při něm byl na kameře vidět pohyb obrazu poškození, zatímco obrazy prachových částic či jiného znečištění zůstaly statické.



Obrázek 2: Poškození křemíkového waferu v pořadí 10. (a, b), 21. (c, d), 25. (e, f) a 26. (g, h), zaznamenané konfokální mikroskopií (a, c, e, g) a CMOS kamerou při osvětlení He-Ne laserem (b, d, f, h).

Nejmenší poškození (26) nebylo detekováno. Lze odhadovat, že při jeho velikosti 5×10

μm^2 již hrál roli limit na základě velikosti pixelu kamery ($7 \mu\text{m}$). Nejmenší detekovatelné poškození (25) mělo rozměry $35 \times 30 \mu\text{m}^2$, na základě čehož lze konstatovat, že limit velikosti velikosti nejmenšího detekovatelného poškození je $35 \mu\text{m}$.

Z hlediska provedeného měření lze konstatovat, že systém detekce je solidní. Na rozdíl od detekčních systémů, které zobrazují vzorek pomocí prošlého, nikoliv odraženého, záření [12], umožňuje tento systém detekci poškození i u netransparentních vzorků. Ve srovnání s detekčními systémy založenými na rozptylu záření umožňuje tento systém poskytnout i informaci o morfologii poškození. Systém je třeba otestovat na transparentních vzorcích, což bude součástí další práce - u nich lze očekávat vznik interferenční struktury, jež může pozitivně i negativně ovlivnit detekci. Z hlediska teoretického limitu na základě velikosti pixelu CMOS kamery by šlo uvažovat i o detekci poškození o velikosti nižším než je $35 \mu\text{m}$ a větším než $10 \mu\text{m}$, bohužel však poškození o dané velikosti nebylo při testování vzorku dostupné.

Závěr

V tomto příspěvku byl představen systém pro detekci laserem vytvořeného poškození pomocí odraženého He-Ne laserového záření, který bude využíván v LIDT stanici v centru HiLASE. Systém umožňuje detekci poškození u netransparentních vzorků s nejmenší velikostí okolo $35 \mu\text{m}$. Dále podává informaci o morfologii a blízkém okolí poškození.

Tato práce byla spolufinancována Evropskou unií a státním rozpočtem České republiky v rámci projektu LasApp CZ.02.01.01/00/22_008/0004573.

Reference

- [1] C. Radier, O. Chalus, M. Charbonneau, S. Thambirajah, G. Deschamps, S. David, J. Barbe, E. Etter, G. Matras, S. Ricaud, *et al.*, “10 pw peak power femtosecond laser pulses at eli-np,” *High Power Laser Science and Engineering* **10**, p. e21, 2022.
- [2] J. Zhu, J. Zhu, X. Li, B. Zhu, W. Ma, X. Lu, W. Fan, Z. Liu, S. Zhou, G. Xu, *et al.*, “Status and development of high-power laser facilities at the nlhplp,” *High power laser Science and Engineering* **6**, p. e55, 2018.
- [3] Y. Wang, S. Wang, A. Rockwood, B. M. Luther, R. Hollinger, A. Curtis, C. Calvi, C. S. Menoni, and J. J. Rocca, “0.85 pw laser operation at 3.3 hz and high-contrast ultrahigh-intensity $\lambda = 400$ nm second-harmonic beamline,” *Optics letters* **42**(19), pp. 3828–3831, 2017.
- [4] X. Ling, G. Wang, Y. Zhao, J. Shao, and Z. Fan, “Laser-induced damage of the optical films prepared by electron beam evaporation and ion beam sputtering in vacuum,” *Optik* **125**(21), pp. 6474–6477, 2014.
- [5] J. Vanda, M. Mydlar, K. Pilna, H. Turcicova, R. Poboril, J. Brajer, T. Mocek, B. Stoklasa, and S. Venos, “Lidt testing as a tool for optimization of processing window for d263 glass sheet tgv treatment,” in *Laser-Induced Damage in Optical Materials 2022*, **12300**, pp. 12–22, SPIE, 2022.
- [6] H. Wang, A. R. Meadows, E. Jankowska, E. Randel, B. A. Reagan, J. J. Rocca, and C. S. Menoni, “Laser induced damage in coatings for cryogenic yb: Yag active mirror amplifiers,” *Optics Letters* **45**(16), pp. 4476–4479, 2020.

- [7] H. Schröder, W. Riede, E. Reinhold, D. Wernham, Y. Lien, and H. Kheyrandish, “In situ observation of uv-laser-induced deposit formation by fluorescence measurement,” in *Laser-Induced Damage in Optical Materials: 2006*, **6403**, pp. 512–522, SPIE, 2007.
- [8] K. R. Kafka, N. Talisa, G. Tempea, D. R. Austin, C. Neacsu, and E. A. Chowdhury, “Few-cycle pulse laser induced damage threshold determination of ultra-broadband optics,” *Optics express* **24**(25), pp. 28858–28868, 2016.
- [9] N. Bartels, P. Allenspacher, and W. Riede, “Laser conditioning of uv anti-reflective optical coatings for applications in aerospace,” in *Laser-Induced Damage in Optical Materials 2018: 50th Anniversary Conference*, **10805**, pp. 205–213, SPIE, 2018.
- [10] D. Wernham, “Optical coatings in space,” in *Advances in Optical Thin Films IV*, **8168**, pp. 104–114, SPIE, 2011.
- [11] G. Liu, D. Kuang, L. Song, C. Xu, and C. Yan, “Mechanism in damage variation of nanosecond laser-induced damage of germanium sheets in vacuum,” *Optics & Laser Technology* **157**, p. 108663, 2023.
- [12] K. Mikami, S. Motokoshi, T. Somekawa, T. Jitsuno, M. Fujita, and K. Tanaka, “A theoretical analysis for temperature dependences of laser-induced damage threshold,” in *Laser-Induced Damage in Optical Materials: 2013*, **8885**, pp. 235–243, SPIE, 2013.
- [13] J. H. Scofield, “Frequency-domain description of a lock-in amplifier,” *American journal of physics* **62**(2), pp. 129–132, 1994.
- [14] M. N. Polyanskiy, “Refractive index database (refractiveindex.info),” 2025. [online]. Dostupné z: <https://refractiveindex.info/> [cit. 2025-09-29].

A Hartree-Fock Analysis of Spherical Nanoparticles in the Jellium Approximation

Michael Píro¹, Jaroslav Hamrle¹

¹Department of Solid State Engineering, Faculty of Nuclear Sciences and Physical Engineering, Czech Technical University, Trojanova 13, Prague, Czech Republic
michael.piro@fjfi.cvut.cz

Abstract

A comprehensive Hartree-Fock analysis of the ground-state electronic structure of spherical gold nanoparticles modeled within the jellium approximation is carried out for all systems containing up to 132 delocalized electrons. Emphasis is placed on resolving the energy-level ordering, properly describing the electron density tail, and assessing the accuracy of local exchange potential. The calculations are performed on a high-resolution real-space grid to ensure numerical precision. Significant discrepancies are observed between the exchange energy given by the Hartree-Fock approximation and the local spin density approximation (LSDA) on the surface and in the outer region of the nanoparticle. To address these differences, a refined expression of the one-electron exchange energy density as an explicit function of the charge density is proposed.

Keywords: Hartree-Fock approximation; jellium model; spherical nanoparticles; electronic structure; exchange energy.

Introduction

Nanoparticles of different sizes and shapes are known to exhibit fundamentally different optical, magnetic, and catalytic properties compared to their bulk material counterparts. These properties arise from the confinement of electrons at the nanoscale and are essential for a wide range of modern technological applications, including drug design and delivery, and bioimaging in medicine, photocatalysis, or surface-plasmon-based sensing. The rapid development of nanofabrication techniques has increased the demand for theoretical models that can accurately predict the behavior of electronic states in nanoparticles with high precision and minimal computational cost.

A complete quantum-mechanical description of multi-electron nanoparticles quickly becomes intractable as system size increases. To address this, simplified models have been developed that still capture the essential physics. One widely used approach is the spherical jellium model, where the discrete ion background is approximated as a uniform positive charge distribution [1, 2]. This model has been particularly successful in describing the delocalized conduction electrons of alkali-metal clusters. The work focused mainly on the use of density functional theory (DFT) methods to calculate energy spectra [3, 4, 5, 6], although several special cases of closed shells in sodium clusters were calculated using the Hartree-Fock approximation [7, 8, 9].

Beyond standard DFT, alternative approaches such as quantum hydrodynamic models (QHD) [10, 11] and quantum-corrected classical models (QCM) [12, 13] have gained traction, particularly in the field of plasmonics. These methods treat the electron fluid collectively, while incorporating quantum effects such as the Bohm potential or pressure

terms derived from the kinetic energy density. They enable simulations of larger systems and dynamical phenomena, but their precision is heavily based on the quality of the input energy functionals.

A common limitation of both the DFT and QHD models lies in the exchange and kinetic energy functionals used. In particular, the local spin density approximation (LSDA) can lose its accuracy significantly on surfaces of spatially confined systems [14]. More advanced generalized gradient approximations (GGAs) such as the Perdew-Burke-Ernzerhof functional (PBE) offer limited improvements when the electron density gradient is small relative to the density itself.

In this work, we address these limitations by explicitly computing the ground-state electronic structure of spherical gold nanoparticles in the finite jellium model using the Hartree-Fock approximation for systems with up to 132 delocalized electrons. Electrons are added one by one to correctly determine the energy-level ordering. Upon analysis of the energy spectra and the shapes of the electron densities, we calculate the one-electron exchange density and find an appropriate fit to express it as a function of the electron density.

We adopt Hartree atomic units throughout the text.

Theory

In the finite spherical jellium model, the nanoparticle is treated as a solid ball of radius R composed of N atoms. Each atom contributes a positively charged ionic core (consisting of the nucleus and tightly bound inner electrons) and ν delocalized electrons. The positive charge is assumed to be uniformly distributed throughout the interior of the ball, resulting in the ionic charge density:

$$n_{\text{I}}(\mathbf{r}) = \begin{cases} n_{\text{I}} & |\mathbf{r}| \leq R \\ 0 & |\mathbf{r}| > R, \end{cases} \quad (1)$$

where n_{I} is the background density constant. The total positive charge, given by $Q = \nu N$, can then be expressed as $Q = \frac{4}{3}\pi R^3 n_{\text{I}}$. Taking into account the original crystalline arrangement of the atoms, the radius R is related to the number of atoms by $R = r_s N^{1/3}$, where r_s is the Wigner-Seitz radius. Substituting this into the expression for Q , the ionic density constant becomes:

$$n_{\text{I}} = \frac{3}{4\pi} \frac{\nu}{r_s^3}. \quad (2)$$

This positive background creates the electrostatic *nanoparticle potential* $V(r)$:

$$V(r) = \begin{cases} \frac{\nu}{r_s^3} \frac{r^2 - 3R^2}{2} & r \leq R \\ -\frac{\nu}{r_s^3} \frac{R^3}{r} & r > R. \end{cases} \quad (3)$$

The parameters r_s and ν depend on the specific material. In this study, we focus on gold atoms, where only the 6s electron is treated as delocalized. This yields $r_s = 3.01$ Bohr and $\nu = 1$.

The system of a single electron in the nanoparticle potential is spherically symmetric. The electron wave function is therefore separated into its angular and radial components:

$$\psi_{nlm}(r, \theta, \phi) = \frac{1}{r} u_{nl}(r) Y_l^m(\theta, \phi), \quad (4)$$

where n , l , and m denote the principal, azimuthal, and magnetic quantum numbers, respectively. Since the angular wave functions $Y_l^m(\theta, \phi)$ are determined analytically and are independent of the shape of the radial potential $V(r)$, we further examine only the radial components.

To address the multi-electron problem, we add the electron-electron interaction to the Hamiltonian. This is given by the potential V_{e-e} , which accounts for all pairwise interactions between electrons:

$$V_{e-e}(\mathbf{r}_1, \dots, \mathbf{r}_N) = \sum_{\substack{i,j=1 \\ i < j}}^N V_2(\mathbf{r}_i, \mathbf{r}_j) = \sum_{\substack{i,j=1 \\ i < j}}^N \frac{1}{|\mathbf{r}_i - \mathbf{r}_j|}. \quad (5)$$

Next, the spatial one-electron wave function is extended to include spin. We consider the electrons to be only fully in the spin-up or spin-down state. The total many-electron wave function is given by the Slater determinant. The interaction potential then decomposes into two distinct contributions: the Hartree potential \hat{V}_H and the exchange potential \hat{V}_x , defined as:

$$\hat{V}_H \psi_i(\mathbf{r}) = \sum_{\substack{j=1 \\ j \neq i}}^N \int_{\mathbb{R}^3} \psi_j^*(\mathbf{r}') V_2(\mathbf{r}, \mathbf{r}') \psi_j(\mathbf{r}') d\mathbf{r}' \psi_i(\mathbf{r}), \quad (6)$$

$$\hat{V}_x \psi_i(\mathbf{r}) = - \sum_{\substack{j=1 \\ j \neq i}}^N \delta_{s_i s_j} \int_{\mathbb{R}^3} \psi_j^*(\mathbf{r}') V_2(\mathbf{r}, \mathbf{r}') \psi_i(\mathbf{r}') d\mathbf{r}' \psi_j(\mathbf{r}), \quad (7)$$

where s_i denotes the spin of the i -th electron. It is important to note that the inclusion of self-interaction terms (contributions with $i = j$) in both \hat{V}_H and \hat{V}_x results in their mutual cancellation, leaving the total electron-electron interaction potential unchanged. This small change is useful for the simplification of further calculations.

The one-electron wave functions are again decomposed into their radial and angular parts, as in Eq. (4), now with the addition of the spin quantum number s to the radial functions. To preserve spherical symmetry of the solution, electrons in partially filled shells are averaged over all quantum numbers m . In this setting, the Hartree and exchange potentials can be expressed as operators acting solely on the radial wave functions u_{nl}^s :

$$\hat{V}_H u_{nl}^s(r) = \sum_{(n', l', s')} N_{n'l'}^{s'} \int_0^{+\infty} u_{n'l'}^{s'}(r')^2 \frac{1}{\max(r, r')} dr' u_{nl}^s(r) \quad (8)$$

and:

$$\hat{V}_x u_{nl}^s(r) = - \sum_{(n', l')} N_{n'l'}^s \sum_{L=|l-l'|}^{l+l'} \begin{pmatrix} l' & L & l \\ 0 & 0 & 0 \end{pmatrix}^2 \int_0^{+\infty} u_{n'l'}^s(r') u_{nl}^s(r') \frac{\min(r, r')^L}{\max(r, r')^{L+1}} dr' u_{n'l'}^s(r), \quad (9)$$

where N_{nl}^s is the number of electrons in the shell (n, l) with spin s .

Results

The spin-dependent one-electron exchange energy density $\varepsilon_x^s(r)$ is defined via the total exchange energy:

$$E_x = 4\pi \sum_s \int_0^{+\infty} \varepsilon_x^s(r) n^s(r) r^2 dr, \quad (10)$$

where $n^s(r)$ is the electron density corresponding to the electrons with spin s . We compare this with the exchange energy calculated from the Hartree-Fock equations using the defining relation of the exchange potential Eq. (9). This yields an expression for ε_x^s in terms of radial wave functions u_{nl}^s :

$$\varepsilon_x^s(r) = -\frac{1}{2} \left[\sum_{(n,l)} N_{nl}^s \sum_{(n',l')} N_{n'l'}^s \sum_{L=|l-l'|}^{l+l'} \begin{pmatrix} l' & L & l \\ 0 & 0 & 0 \end{pmatrix}^2 \cdot \int_0^{+\infty} u_{nl}^s(r') u_{n'l'}^s(r') \frac{\min(r, r')^L}{\max(r, r')^{L+1}} dr' u_{nl}^s(r) u_{n'l'}^s(r) \right] / \sum_{(n,l)} N_{nl}^s u_{nl}^s(r)^2. \quad (11)$$

To find an approximate form of the exchange energy density as an explicit function of the electron density, we construct a parametric plot of $\varepsilon_x^s(r)$ versus $n(r)$ (Fig. 1a). Within the nanoparticle, both n and ε_x^s exhibit non-monotonic behavior, resulting in a cyclic trajectory in the parametric plot. However, these spirals are sufficiently flat to be well approximated by a monotonic functional dependence. To account for possible differences between the inner and outer regions, we fit the energy density function separately. For the interior of the nanoparticle, we use a class of power-law functions of the form:

$$f(x; A, \alpha) = -A x^\alpha. \quad (12)$$

This provides a good model for most of the inner section, but it loses accuracy near the boundary $r = R$. In the outer region, no valid fit that provides a meaningful approximation using this function can be found. To address this, we introduce a second family of exponential-type functions of the form:

$$g(x; B, C, \beta) = -\exp(B x^\beta - C). \quad (13)$$

This yields an excellent fit in the outer and near-boundary inner regions, precisely where the power-law approximation fails.

In order to obtain a general formula, we fit both functional classes to the exchange potentials calculated for nanoparticles with up to 132 electrons. Importantly, deviations of the parameters B and C tend to cancel out, providing better stability of the fit. We can therefore define the model of the one-electron exchange energy density for both spin orientations as:

$$\varepsilon_x^s(r) = \min(-A n(r)^\alpha, -\exp(B n(r)^\beta - C)), \quad (14)$$

where the coefficients are taken as averages over the cases with fully filled orbitals. The specific values of the means and their standard deviations are as follows:

$$A = 0.670 \pm 0.067, \quad \alpha = 0.304 \pm 0.024 \quad (15)$$

$$B = 4.25 \pm 0.57, \quad C = 3.91 \pm 0.58, \quad \beta = 0.110 \pm 0.022. \quad (16)$$

A comparison of the exchange energy density with the LSDA and PBE functions for $N = 132$ is shown in Fig. 1b. Based on the coefficients A and α , Eq. (15), we see that LSDA correctly predicts the dependence of the exchange energy density inside the nanoparticle, but underestimates its effect in the outer region. Furthermore, because of the negligible relative gradient of the electron density, PBE does not bring any improvement in the exchange energy density.

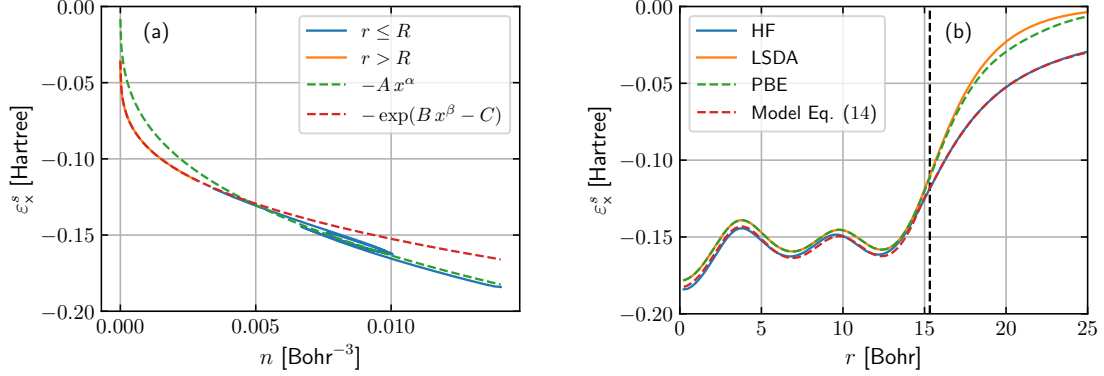


Figure 1: (a) Dependence of the one-electron exchange energy density $\varepsilon_x^s(r)$ on the electron density $n(r)$. The blue color indicates the inner region of the nanoparticle ($r \leq R$), and orange the outer region ($r > R$). Green and red dashed curves represent the fitted functions f and g , with parameters $A = 0.733$, $\alpha = 0.326$, $B = 3.80$, $C = 4.23$, and $\beta = 0.104$. (b) One-electron exchange energy density ε_x^s calculated by the Hartree-Fock approximation (HF) compared to the models given by LSDA, PBE, and Eq. (14), $N = 132$. Vertical dashed line represents the nanoparticle boundary.

Conclusion

We have presented a detailed Hartree-Fock analysis of the ground-state electronic structure of spherical gold nanoparticles within the jellium approximation. The primary objective was to study the behavior of the exchange energy and to assess the reliability of local models for the exchange energy potential.

Based on the calculated electronic structure, we propose an improved analytic expression for the one-electron exchange energy density as an explicit function of the electron density. While the exchange energy maintains the expected $n^{1/3}$ dependence within the nanoparticle, near the surface and beyond, the exchange behavior requires an additional exponential-type model.

This work establishes the foundation for accurate modeling of spherically symmetric confined electronic systems. The proposed exchange and kinetic energy functionals offer potential improvements for classical or orbital-free DFT, quantum hydrodynamics, and semi-classical models. Future investigations will address the incorporation of electron correlation effects and the extension of the model to include structural details.

Acknowledgement

This work was supported by the FerrMion project of the Czech Ministry of Education, co-funded by the EU, Project No. CZ.02.01.01/00/22_008/0004591; by the Czech Science Foundation (GAČR), Project No. 21-05259S; and by the Student Grant Competition of the Czech Technical University in Prague (SGS), Project No. SGS24/146/OHK4/3T/14.

References

- [1] N. D. Lang and W. Kohn. Theory of metal surfaces: Charge density and surface energy. *Phys. Rev. B*, 1:4555–4568, Jun 1970.
- [2] Matthias Brack. The physics of simple metal clusters: self-consistent jellium model and semiclassical approaches. *Rev. Mod. Phys.*, 65(3):677, 1993.
- [3] W. Ekardt. Work function of small metal particles: Self-consistent spherical jellium-background model. *Phys. Rev. B*, 29:1558–1564, Feb 1984.
- [4] W. Ekardt. Dynamical polarizability of small metal particles: Self-consistent spherical jellium background model. *Phys. Rev. Lett.*, 52:1925–1928, May 1984.
- [5] F. R. Redfern, R. C. Chaney, and P. G. Rudolf. Self-consistent electronic structure of lithium clusters. *Phys. Rev. B*, 32:5023–5031, Oct 1985.
- [6] WD Knight, Walt A De Heer, Winston A Saunders, Keith Clemenger, MY Chou, and Marvin L Cohen. Alkali metal clusters and the jellium model. *Chem. Phys. Lett.*, 134(1):1–5, 1987.
- [7] C. Guet and W. R. Johnson. Dipole excitations of closed-shell alkali-metal clusters. *Phys. Rev. B*, 45:11283–11287, May 1992.
- [8] Michael S Hansen and Hidetoshi Nishioka. Exchange effects on electronic states in jellium clusters. *Z. Phys. D*, 28:73–80, 1993.
- [9] M Madjet, C Guet, and WR Johnson. Comparative study of exchange-correlation effects on the electronic and optical properties of alkali-metal clusters. *Phys. Rev. A*, 51(2):1327, 1995.
- [10] Cristian Ciraci and Fabio Della Sala. Quantum hydrodynamic theory for plasmonics: Impact of the electron density tail. *Phys. Rev. B*, 93:205405, May 2016.
- [11] Qiang Zhou, Wancang Li, Zi He, Pu Zhang, and Xue-Wen Chen. Quantum hydrodynamic model for noble metal nanoplasmonics. *Phys. Rev. B*, 107:205413, May 2023.
- [12] Ruben Esteban, Andrei G Borisov, Peter Nordlander, and Javier Aizpurua. Bridging quantum and classical plasmonics with a quantum-corrected model. *Nat. Commun.*, 3(1):825, 2012.
- [13] Mario Zapata, Ángela S Camacho Beltrán, Andrei G Borisov, and Javier Aizpurua. Quantum effects in the optical response of extended plasmonic gaps: validation of the quantum corrected model in core-shell nanomaterials. *Opt. Express*, 23(6):8134–8149, 2015.
- [14] E. Krotscheck and W. Kohn. Nonlocal screening in metal surfaces. *Phys. Rev. Lett.*, 57:862–865, Aug 1986.

Preparation and analysis of multilayer metal - dielectric systems by PVD methods

Jáchym Lis^{1,2}, J. Skočdopole¹, J. Bulíř², L. Kalvoda¹, L. Fekete²

¹Department of Solid State Engineering, Faculty of Nuclear Sciences and Physical Engineering, Czech Technical University in Prague

²Institute of Physics of the Czech Academy of Sciences
lisjachy@cvut.cz

Abstract

To develop the use of hydrogen technologies in the energy sector, it is necessary to ensure their safety by developing high-quality hydrogen sensors. In this work, two principles of optical sensors exploiting metal-dielectric interface phenomena in multilayer thin film structures are investigated, specifically the combination of a thin silver layer with a very thin palladium layer for excitation of the surface plasmon-polariton and the combination of silver, a dielectric intermediate layer and a very thin palladium layer for excitation of the waveguide mode. The samples were prepared by Magnetron Sputtering and Ionized Jet Deposition methods. The analysis of the samples was carried out using ellipsometry, Attenuated Total Reflection method, atomic force microscopy and computer simulations. The functionality of the sensor structures was analyzed by in operando ellipsometric analysis of the palladium thin film and simulation of the sensor behavior based on the variation of the palladium layer parameters. The structure functioning on the basis of surface plasmon-polaritons was found to be a suitable candidate for further development of the hydrogen sensor.

Keywords: Surface Plasmon-polariton; Ionized Jet Deposition; Magnetron Sputtering; thin films.

Introduction

In the past two decades, plasmonic has progressed to a mature technology allowing the manipulation of light in various applications, including sensorics. Plasmonic oscillations are oscillations of free electron gas in metals, which strongly influence the optical properties (reflectancy and transmittancy) of thin metal layers. Plasmonic sensors offer a versatile state-of-the-art optical sensors which can be used for example as distributed gas sensors with very high sensitivity and low detection limit, as typical for surface plasmon-polaritons sensors[1].

As plasmonic properties rely on free electron gas, the elements from I.B. group - Cu, Ag, Au - whose metal phases exhibit high free electron concentrations, play an important role in plasmonic structures. It is necessary to investigate the manufacturing of plasmonic Ag layers, which are often used as a base layer in plasmonic multilayer structures in sensorics due to Ag's superior plasmonic properties.

We investigated not only structures functioning on the basis of surface plasmon-polariton, but also on the basis of waveguide mode excited in a layer of dielectricum (Si_3N_4 , SiO_2 and TiO_2) which in our simulations showed even greater theoretical sensitivity.

Ionized jet deposition method (IJD) is a novel method belonging to the group of physical vapor deposition (PVD) techniques. The method is based on generating short pulses of electrons with energies between 5 – 20 kV, which ablate the target material in an evacuated chamber. The plasma plume of the target material then travels across the chamber towards the substrate and forms the thin film. Due to its simplicity and relatively low operating expenses, the IJD method is a good candidate for upscaling and industrial use of thin films deposition.

We investigated the optimal multilayer structures using computer simulations on the basis of the Transfer Matrix method. We investigated the manufacturing of plasmonic Ag thin films using the IJD method and optimized deposition parameters to create films with desired thickness and surface properties. We compared our samples with plasmonic Ag layers manufactured using the well-established Magnetron sputtering (MS) method. We created multiple sample series both on the basis of surface plasmon-polariton and waveguide mode using both of the deposition methods, different dielectric materials and different thicknesses of each layer. We analyzed the samples using Ellipsometry, Attenuated Total Reflection method and Atomic Force Microscopy. We compared the obtained results with computer simulations using the Transfer Matrix method. We tested the possible functionality of the sensor by in operando ellipsometric analysis of 10 nm Pd film in increasing H₂ pressure and computer simulation of the sensor behavior based on the observed variations of the Pd layer parameters.

Materials and Methods

Computer simulations. The optimal layer configurations were determined using computer simulations of Attenuated Total Reflection method in the used configuration. The simulations were conducted using the tmm Python package¹ in version 0.1.8 utilizing the Transfer Matrix Method.

Substrate, deposition material. Common laboratory glass and fused silica were used as substrates. Pure Ag targets were used for the deposition of thin Ag films.

Ionized Jet Deposition. The IJD deposition system JetDep 100 (manufactured by Noivion s. r. o. and Czech Vacuum s. r. o., Czech Republic) was used in the preparation of thin Ag films. The IJD deposition parameters common for all prepared samples were as follows: The pulse frequency was set to 100 Hz, the distance between substrate and target was set to 110 mm, the distance between the IJD head and target was set to 3 mm. The mean primary electron beam spot diameter amounted to 1 mm on the target. The substrate had room temperature. A gas mixture of Ar+6 vol. % H₂ was used as the IJD working gas (purity 99.999%, provided by Linde Technoplyn, s.r.o., Czech Republic) for the deposition of silver. For the deposition of SiO₂ and TiO₂ pure Si and Ti targets were used in the combination with O₂ as the IJD working gas (purity 99.999%, provided by Linde Technoplyn, s.r.o., Czech Republic) The initial pressure before deposition and the working pressure were set in the range of $(2, 7 - 9, 2) \times 10^{-3}$ Pa and $(2, 4 - 7, 5) \times 10^{-2}$ Pa, respectively. The deposition voltage was varied between 10 – 17 kV and deposition time between 1, 5 – 40 min.

Magnetron Sputtering. The control samples of thin Ag films were prepared using magnetron sputtering system installed in the Institute of Physics, Czech Academy of

¹<https://pypi.org/project/tmm/>

Sciences. The RF source power was set to 100 W, the sputtering target was water-cooled and substrate was at a room temperature. The working pressure was set to 1 Pa, Ar, O₂ and N₂ were used as the working gases. The gases were of purity 99.999%, provided by Linde Technoplyn, s.r.o., Czech Republic. Predeposition of AgO_x was performed by using a mixture of Ar and O₂ in the ratio of 2 : 1 for 4 s. Ag layers were deposited in pure Ar atmosphere. Si₃N₄ layers were deposited using a mixture of Ar and N₂ in the ratio of 1 : 1. Between each deposition step a pre-deposition was performed to remove cross-contamination from the targets. The deposition process was performed in one chamber without exposing the sample to the air. In operando Ellipsometry was used to control the parameters of deposited layers between each step.

Sample analysis. The optimal layer thicknesses were obtained by computer simulations using the tmm Python package² in version 0.1.8. The thickness and relative permittivity of each layer were analyzed using Ellipsometry method (M-2000X manufactured by J. A. Woollam Co., Inc) and CompleteEASE software in version 6.56. The results of Attenuated Total Reflection method in the Kretschmann configuration (laser $\lambda = 632,8$ nm, BK7 prism and photodiode detector), which allowed for direct observations of the surface plasmon-polariton and the waveguide mode, were compared with simulations using the data obtained by the Ellipsometry method and the tmm Python package. The root mean square (RMS) roughness was analyzed using Atomic Force Microscopy. The sensor functionality was analyzed by in operando ellipsometric analysis of a 10 nm Pd layer in a chamber with continually increasing H₂ pressure.

²<https://pypi.org/project/tmm/>

Results and Discussion

The computer simulations determined the best layer configuration for the surface plasmon-polariton mode being 40 nm of Ag and 1 nm of Pd. For the waveguide mode, the computer simulations determined the the best layer configuration being 50 nm of Ag, dielectric layer with such thickness that the optical thickness is half the wavelength of the light used in the ATR measurement ($\lambda = 632,8 \text{ nm}$) and 1 nm of Pd.

The waveguide mode offers much better theoretical sensitivity than the surface plasmon-polariton mode due to the much narrower reflectivity dip. However, in this mode there are bigger challenges in creating smooth enough layers.

The experiments confirmed validity of the simulations.

A total of 9 samples were manufactured using the Magnetron sputtering method, 6 of them being Ag-Pd multilayer systems, 2 of them being Ag-Si₃N₄-Pd multilayer systems and 1 being a 10 nm Pd layer for the purpose of measuring the change of Pd optical constants during hydrogen absorption. A total of 5 Ag-dielectric multilayer systems were manufactured using the IJD method with dielectrics being SiO₂ and TiO₂. The silver thickness was ranging between 33 – 65 nm, the dielectric thickness was ranging between 159 – 577 nm and Pd thickness between 1 – 3 nm.

For the best sensitivity it is necessary to create the Pd layer as thin as possible, 1 nm or less. Meanwhile, such thin layer does not suffer damage from stress induced by change of lattice parameters when absorbing hydrogen. For best results in the waveguide mode it is good to use nitride based dielectrics, because oxide dielectric growth leads to oxidizing surface of the silver.

Using the ATR method, it was possible to excite the surface plasmon-polaritons in corresponding samples; however, the excitation of the waveguide mode was possible only on one of three samples with corresponding layer combination and thicknesses. The ATR measurements of both surface plasmon-polaritons and waveguide mode corresponded to a certain extent to simulations based on data measured on each sample using ellipsometry, see figures 1 and 2

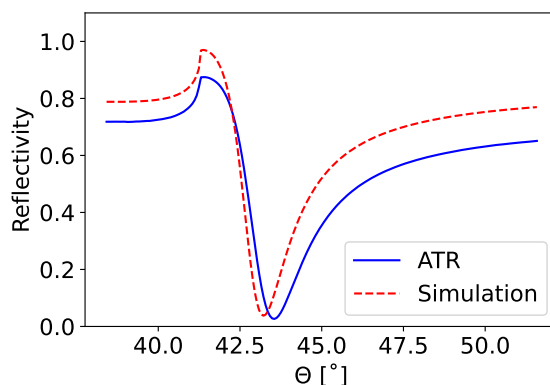


Figure 1: Comparison of surface plasmon-polariton measured by ATR and simulated using ellipsometry data on the same sample

The slight mismatch of ATR data and simulations of the drop in reflectivity caused by surface plasmon-polariton is probably caused by roughness of the layers and their interfaces. The drop in reflectivity caused by the waveguide mode is much wider and not

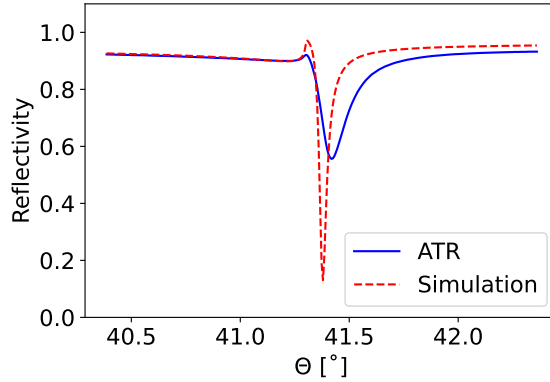


Figure 2: Comparison of waveguide mode measured by ATR and simulated using ellipsometry data on the same sample.

so deep than the simulation. That is probably caused by the roughness of the layers and the fact that the waveguide mode is extremely sensitive to it.

The average roughness of the layers prepared by magnetron sputtering for the excitation of the surface plasmon-polariton was $(1, 1 \pm 0, 3)$ nm and for the samples for waveguide mode excitation it was $(3, 8 \pm 0, 2)$ nm. The roughness was increased because of the Si_3N_4 layer, because the other two, Ag and Pd were prepared with the same parameters in both cases. The average roughness of the samples prepared by IJD was (13 ± 9) nm. This is caused by the fact that the material plasma condensates and creates small balls on the surface of the film. The roughness of the layer still needs to be minimised, even in the case of the Magnetron Sputtering method. Minimalisation of the roughness is necessary for enabling the possibility of creating the waveguide mode based sensor, as the current achieved roughness is distorting the waveguide mode.

The simulation of ATR measurement of both surface plasmon-polariton and waveguide mode based sensors when absorbing H_2 showed that the drop in reflectivity caused by surface plasmon-polariton shifts in dependence on the change of dielectric function of the Pd layer and the waveguide mode shifts in dependence on cca 10% increase in thickness of the Pd layer.

The in operando ellipsometric analysis of a 10 nm Pd layer in a chamber continuously filled with H_2 showed change in the Pd dielectric function between 0 – 5kPa of H_2 . The data were obtained with the thickness of the layer constant, because the thickness fit didn't show physically meaningful behavior. Using the obtained data, we simulated the ATR measurement of both surface plasmon-polariton and waveguide mode based sensors. The simulated surface plasmon-polariton showed the expected shift due to the change of the Pd dielectric function (see fig 3), while the waveguide mode showed little change because of the impossible thickness change fit.

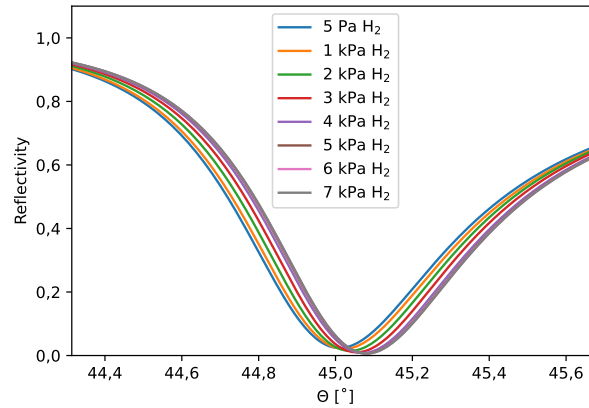


Figure 3: Simulated ATR measurement of a surface plasmon-polariton based sensor using dielectric function change obtained by in operando ellipsometric analysis for a Pd layer.

Conclusions

We proposed the optimal layer configuration for both the surface plasmon-polariton and waveguide mode based sensor. We tested deposition of such structures using RF Magnetron Sputtering and Ionized Jet Deposition methods. The analysis showed acceptable results in exciting the surface plasmon-polaritons, whereas the preparation of waveguide mode sensors needs to be further optimized in terms of roughness. The hydrogen absorption behavior was semi-experimentally proved but it needs to be further tested and verified by preparation and testing of real sensor structure. The further research should focus on decreasing the roughness of prepared layers because it is a crucial parameter for achieving good results in the excitation of both the surface plasmon-polariton and waveguide mode.

References

- [1] J. Homola. Surface Plasmon Resonance Based Sensors. *Springer Berlin*, Heidelberg; 2006.

Acknowledgement

This work was supported by the Grant Agency of the Czech Technical University in Prague, grant No. SGS25/168/OHK4/3T/14.

Úhlově rozlišená spektroskopie Brillouinova-Mandelštamova rozptylu světla pro měření elastické anizotropie safíru

Zuzana Soudná¹

¹ Katedra inženýrství pevných látek, Fakulta jaderná a fyzikálně inženýrská, České vysoké učení technické v Praze

Abstrakt

Brillouinova–Mandelštamova spektroskopie rozptylu světla označuje neelastický rozptyl světla na spontánních nebo koherentně excitovaných elementárních excitacích, v tomto případě na tepelných fononech. V příspěvku představujeme adaptaci této metody pro určení elastické anizotropie safíru, který slouží jako modelový příklad silně anizotropního transparentního materiálu. Význam metody diskutujeme ve srovnání s dalšími technikami používanými pro charakterizaci elasticity.

Klíčová slova: Brillouinova-Mandelštamova spektroskopie; RI θ A konfigurace; akustické fonony; safír

Úvod

K charakterizaci elasticity materiálů je možné využít různé techniky, kromě zmíněné Brillouin–Mandelštamovy spektroskopie (BMS) například také spektroskopii s přechodovou mřížkou (transient grating spectroscopy; TGS) a rezonanční ultrazvukovou spektroskopii (RUS). V závislosti na fyzikálním principu těchto technik se liší jak požadavky kladené na vzorky, tak i typ módů, které se promítají do detekovaného signálu, povaha tohoto signálu a s tím související způsob zpracování. Stručný přehled nejzásadnějších rozdílů je uveden v tabulce 1.

Z těchto technik je BMS jediná spontánní, poskytuje tedy informaci o samotném materiálu bez nutnosti vnějšího buzení. V popisované konfiguraci RI θ A (reflection-induced θ two-angle) jako jediná umožňuje získat informaci jak o podélných, tak i o transverzálních objemových módech, aniž by kladla přísné geometrické požadavky na tvar vzorku. V tomto smyslu tedy spojuje výhody obou zbývajících metod. Signál je navíc detekován přímo ve frekvenční doméně, díky čemuž není nutná další transformace, a zároveň z něj lze získat i informaci o fotoelastických vlastnostech zkoumaného materiálu.

Teorie

Základním principem BMS je Dopplerův posun světla rozptýleného na akustických fononech, které se v materiálu spontánně šíří. Díky tomuto jevu je možné získat informace o elastických vlastnostech zkoumaných materiálů [1]. Frekvenční posun $\Delta\nu$ rozptýleného světla je přímo úměrný rychlosti fononů v a závisí na indexu lomu n , směru šíření vlny a měřicí konfiguraci. Ta je definována pomocí úhlu rozptylu θ a vlnové délky dopadajícího světla λ [2]. V obecné konfiguraci má vztah pro frekvenční posun následující tvar:

$$\Delta\nu = \frac{2nv}{\lambda} \sin\left(\frac{\theta}{2}\right). \quad (1)$$

Tabulka 1: Vybrané metody používané ke stanovení elasticity; symbol * označuje techniky dostupné na pracovišti autorky, symbol ★ značí vlastnost vyžadovanou pro RUS na daném pracovišti, ačkoliv již existují metody umožňující aplikaci na nepravidelný tvar vzorku [4]

metoda	typ/ konfigurace	požadavky na vzorek	získaná informace	způsob vyvolání odezvy
RUS*	/	transparentní i netransparentní, s pravidelným tvarem★	rezonanční módy objemových transverzálních a podélných vln	stimulovaná mechanická rezonance
TGS	absorpční*	netransparentní, s povrchem leštěným na optickou kvalitu	časový signál povrchových akustických vln	stimulovaná pump-probe
	transmisní[5]	transparentní, s povrchem leštěným na optickou kvalitu	časový signál podélných objemových vln	stimulovaná pump-probe
BMS	RIθA*	transparentní, s povrchem leštěným na optickou kvalitu	frekvence podélných i smykových objemových akustických vln; fotoelastooptika	/ (spontánní)

Nejběžněji používanou geometrií je konfigurace na zpětný odraz (backscattering, BSC, 180°), nicméně v této práci je použita tzv. RIθA (reflection-induced θA two-angle) konfigurace [3]. V ní volně vložené zrcátko pod transparentní vzorek umožňuje simultánní měření právě v konfiguraci na zpětný odraz a konfiguraci 90A [6]. Z obecného vztahu 1 lze tyto dva speciální případy odvodit, vztah závislý na indexu lomu pro konfiguraci BSC:

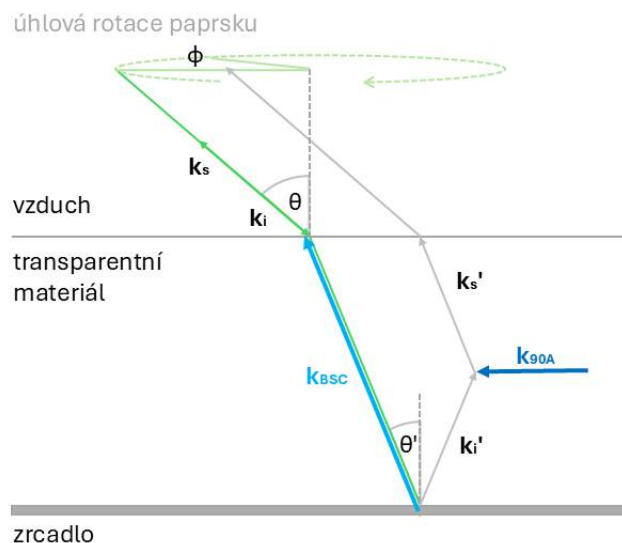
$$\Delta\nu_{BSC} = \frac{2n\nu_{BSC}}{\lambda}. \quad (2)$$

a vztah nezávislý na indexu lomu pro konfiguraci 90A:

$$\Delta\nu_{90A} = \frac{\sqrt{2}\nu_{90A}}{\lambda}. \quad (3)$$

Výhodou je nejen získání většího množství informací z jediného měření, ale také to, že v závislosti na konfiguraci dochází k preferenční interakci laserového paprsku s odlišně orientovanými fonony - 90A geometrie je vhodná především pro in-plane vlny, zatímco BSC pro out-of-plane vlny, viz obrázek 1. Protože u jedné z konfigurací není nutné znát index lomu, lze jej v případě neznalosti určit srovnáním výsledků obou konfigurací.

Experimentální uspořádání zahrnuje laserový zdroj, který generuje monochromatické záření, jež je pomocí optického systému fokusováno na povrch vzorku. Stejný optický systém zároveň zachycuje rozptýlené světlo, které je dále analyzováno pomocí tandemového Fabry–Pérotova (TFP) interferometru tvořeného dvěma za sebou řazenými dutinami (FP1, FP2). Každou dutinu tvoří dvojice rovnoběžných polopropustných zrcadel; jedno zrcadlo z každé dvojice je uchyceno na společném posuvném stolku, druhé na sa-



Obrázek 1: Schéma RI θ A konfigurace, kde θ je úhel dopadu laserového paprsku ve vzduchu a θ' odpovídající úhel v prostředí s indexem lomu n . \mathbf{k}_i je vlnový vektor dopadajícího laserového paprsku a \mathbf{k}_i' jeho odraz od zrcadla. \mathbf{k}_s a \mathbf{k}_s' označují vektory rozptýleného záření. Fonon \mathbf{k}_{BSC} je detekován v konfiguraci na zpětný odraz a fonon $\mathbf{k}_{90\text{A}}$ v konfiguraci 90A. Úhel ϕ označuje rotaci laserového paprsku kolem normály povrchu vzorku.

mostatném držáku. Optické osy obou dutin svírají malý úhel θ , takže při posuvu stolkem se jejich mezery d_1 a d_2 (fyzické vzdálenosti zrcadel) mění synchronně v pevném poměru, přičemž platí $d_1 \neq d_2$. Přenos nastává pouze tehdy, když obě dutiny současně splní rezonanční podmínku [7]:

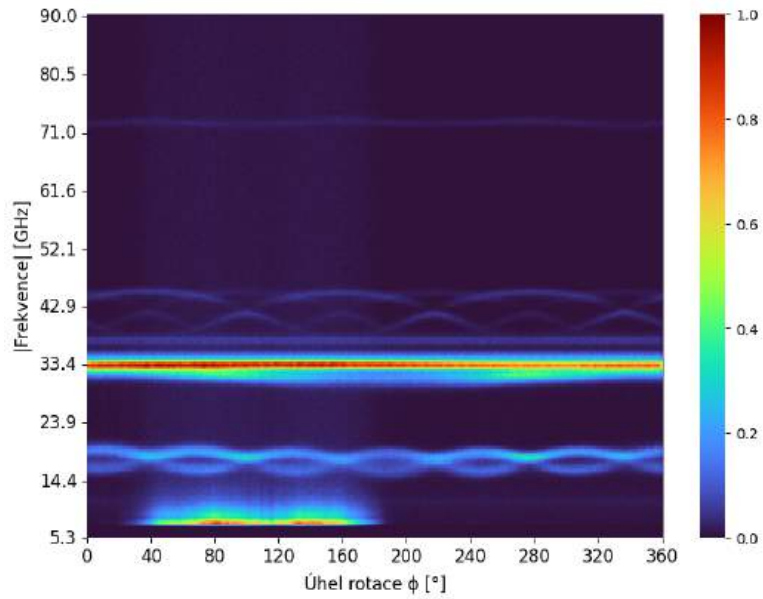
$$nd_i = m_i \frac{\lambda}{2}, \quad i \in \{1, 2\}, \quad (4)$$

kde n je index lomu mezi zrcadly, λ je vlnová délka dopadajícího záření a m_i jsou celá čísla. Díky mírně odlišným mezerám se sousední řády v obou dutinách nekryjí a neprojdou; ve spektru po nich zůstávají jen slabí „duchové“. Volbou rezonující vlnové délky – v praxi skenem mezer d_1, d_2 posuvem stolku – lze s vysokou přesností analyzovat malé frekvenční posuny rozptýleného světla. Intenzita transmittovaného signálu je pak zaznamenávána detektorem jako funkce frekvence.

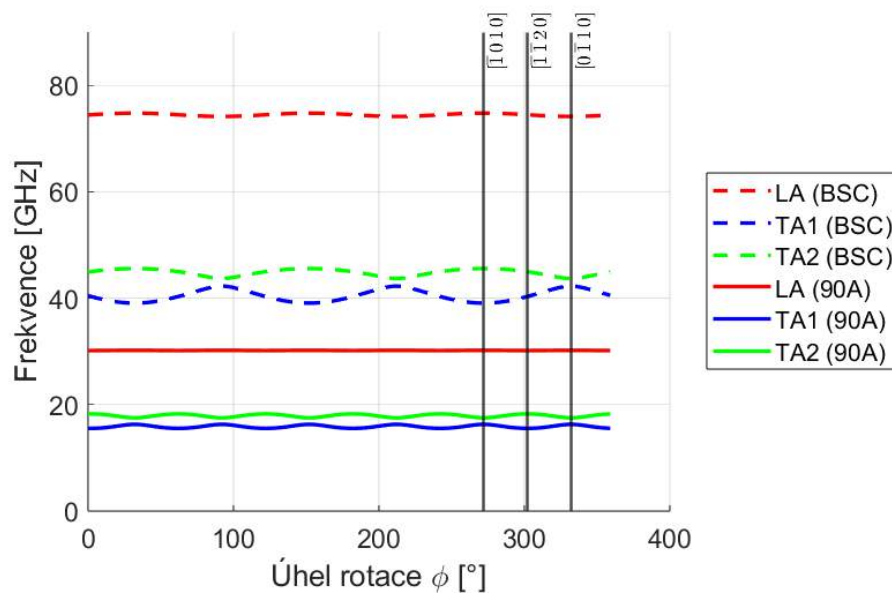
Typické Brillouinovy posuny v pevných látkách dosahují zpravidla několika jednotek až desítek GHz v závislosti na elastických vlastnostech materiálu, indexu lomu a měřicí geometrii. Jelikož elastický tenzor závisí na krystalografické symetrii, je pro jeho úplné určení nezbytné změřit spektra pro sadu úhlů ϕ odpovídajících různým krystalografickým směrům.

Výsledky a diskuze

Vzorek safíru (0001), chemickým vzorcem Al_2O_3 , jsme změřili Brillouinovou-Mandelštamovou spektroskopii za pokojové teploty v konfiguraci RI θ A pro sadu úhlů $\phi = 0^\circ - 359^\circ$, aby bylo možné sledovat elastickou anizotropii. Protože je Brillouinovo-Mandelštamovo spektrum



(a) Experimentálně naměřená frekvenční mapa $\text{Al}_2\text{O}_3(0001)$ (normalizovaná) pro jednu úplnou 360° rotaci



(b) Simulovaná frekvenční mapa $\text{Al}_2\text{O}_3(0001)$ pro jednu úplnou 360° rotaci v konfiguracích na zpětný odraz (BSC) a 90A; LA - podélná vlna, TA1, TA2 - transverzální vlny; úhlům 272° , 302° a 332° ve frekvenční mapě odpovídají konkrétní krystalografické směry $[\bar{1}010]$, $[\bar{1}\bar{1}20]$ a $[0\bar{1}10]$.

Obrázek 2: Frekvenční mapa pro různé úhly rotace safíru (0001).

u materiálů splňujících časovou reverzibilitu (kam safír, na rozdíl od mnoha magnetických materiálů, patří) symetrické vůči počátku, zprůměrovali jsme záporné a kladné větve spektra a tyto výsledné hodnoty jsme vykreslili do frekvenční mapy zobrazené na obrázku 2a.

Vycházíme-li ze zvolené měřicí geometrie, povahy šíření akustických vln a z krystalografické symetrie i orientace vzorku, lze jednotlivé módy předběžně přiřadit takto: módy s vyššími frekvencemi, z nichž některé vykazují trojnásobnou periodicitu v úhlu ϕ (120°), odpovídají out-of-plane vlnám detekovaným na zpětný odraz, zatímco módy s nižšími frekvencemi se šestinásobnou periodicitou (60°) jsou in-plane vlny měřené v konfiguraci 90A. V každé sadě je čára s nejvyšší frekvencí (tj. s nejvyšší fázovou rychlostí) podélný mód (LA). K potvrzení těchto přiřazení a k rozlišení transversálních módů (TA) je však nutné porovnání s kvantitativní simulací.

Takovou simulaci jsme získali řešením Christoffelovy rovnice pro danou orientaci safíru se známými materiálovými parametry: tenzorem elasticity

$$\mathbf{C} = \begin{pmatrix} C_{11} & C_{12} & C_{13} & C_{14} & 0 & 0 \\ C_{12} & C_{11} & C_{13} & -C_{14} & 0 & 0 \\ C_{13} & C_{13} & C_{33} & 0 & 0 & 0 \\ C_{14} & -C_{14} & 0 & C_{44} & 0 & 0 \\ 0 & 0 & 0 & 0 & C_{44} & 0 \\ 0 & 0 & 0 & 0 & 0 & \frac{C_{11}-C_{12}}{2} \end{pmatrix} = \begin{pmatrix} 511.9 & 166.65 & 123.14 & 23.42 & 0 & 0 \\ 166.65 & 511.9 & 123.14 & -23.42 & 0 & 0 \\ 123.14 & 123.14 & 522.54 & 0 & 0 & 0 \\ 23.42 & -23.42 & 0 & 150.89 & 0 & 0 \\ 0 & 0 & 0 & 0 & 150.89 & 0 \\ 0 & 0 & 0 & 0 & 0 & 172.625 \end{pmatrix} \text{ GPa,}$$

a hustotou $\rho = 3980 \text{ kg} \cdot \text{m}^{-3}$. Získané rychlostní mapy jsme následně převedli na mapy frekvenční užitím vztahů 2 a 3, kde jsme dosadili index lomu $n = 1.77$ a vlnovou délku laseru $\lambda = 532 \text{ nm}$. Jak je patrné z obr. 2, pozorované frekvence jsou v dobré shodě s predikcí, což umožňuje jednoznačnou interpretaci experimentálních dat.

Dominantním je in-plane signál akustických vln detekovaný v konfiguraci 90A: pozorujeme dvě smykové vlny (TA_1 , TA_2) v rozmezí 15–20 GHz, odrážející hexagonální symetrii bazální roviny, a podélný mód (LA) s frekvencí kolem 33 GHz s jen slabou úhlovou závislostí.

Signál out-of-plane akustických vln detekovaných na zpětný odraz je zřetelně slabší; ve frekvenční mapě jsou rozlišitelné opět dvě smykové vlny, tentokrát v rozsahu 40–45 GHz, odrážející trigonální symetrii krystalu, a velmi slabý podélný mód přibližně na 73 GHz.

Závěr

V této práci jsme představili adaptaci Brillouinovy–Mandelštamovy spektroskopie (BMS), která poskytuje srovnatelně bohaté informace jako techniky RUS a TGS a navíc umožňuje přímé měření fázových rychlostí akustických módů. Na monokrystalu safíru (Al_2O_3) jakožto zástupci elasticky anizotropních transparentních materiálů bylo ukázáno, že úhlově rozlišená BMS v konfiguraci $\text{RI}\theta\text{A}$ poskytuje detailní informace o šíření jak podélných, tak i smykových akustických vln. Výsledky se dobře shodují s teoretickou predikcí na základě známých elastických konstant, a ukazují, že BMS představuje cenný nástroj pro studium elastických vlastností transparentních materiálů.

Reference

- [1] Carlotti, G. Elastic Characterization of Transparent and Opaque Films, Multilayers and Acoustic Resonators by Surface Brillouin Scattering: A Review. *Appl. Sci.* **2018**, *8* (1), 124. doi:10.3390/app8010124
- [2] Kojima, S. 100th Anniversary of Brillouin Scattering: Impact on Materials Science. *Materials* **2022**, *15* (10), 3518. doi:10.3390/ma15103518
- [3] Kenzo, H.; Matsukawa, M.; Ohtori, N. "Two-Pass" Brillouin Scattering Geometry for the Investigation of Opto-Acoustic Properties of Thin Films. *Japanese Journal of Applied Physics* **2003**, *42* (9A), 5865–5866. doi: 10.1143/JJAP.42.5865
- [4] Theuss, F.; de la Fuente Simarro, G.; Shraga, A.; Grissonnanche, G.; Hayes, I. M.; Saha, S.; Shishidou, T.; Chen, T.; Nakatsuji, S.; et al. Resonant Ultrasound Spectroscopy for Irregularly Shaped Samples and Its Application to Uranium Ditetelluride. *Physical Review Letters* **2024**, *132* (6), 066003. doi:10.1103/PhysRevLett.132.066003
- [5] Maznev, A. A.; Nelson, K. A.; Rogers, J. A. Optical Heterodyne Detection of Laser-Induced Gratings. *Optics Letters* **1998**, *23* (16), 1319–1321. doi:10.1364/OL.23.001319
- [6] Philipp, M.; Müller, U.; Sanctuary, R.; Seck, P.; Krüger, J.-K. Scanning Brillouin Microscopy: Acoustic Microscopy at Gigahertz Frequencies. *Archives des Sciences Naturelles, Physiques et Mathématiques* **2012**, *NS 46*, Special volume (Invited Review Article).
- [7] Polian, A. Brillouin Scattering at High Pressure: An Overview. *Journal of Raman Spectroscopy* **2003**, *34* (8–9), 633–637. doi:10.1002/jrs.1031.

Poděkování

Tato práce byla podpořena grantem Studentské grantové soutěže ČVUT č. SGS25/168/OHK4/3T/14.

Využití AI

Model ChatGPT 5 (OpenAI, 2025, *ChatGPT 5 (Sept. 1 version)*) [Velký jazykový model], <https://chat.openai.com/>) byl využit k naformátování zdrojů v jednotném citačním stylu, kontrole gramatiky a úpravě stylistiky.

Diffusion Dynamics in Ecological Concrete Studied by Neutron Imaging

J. Zelenka¹, M. Dráb, S¹. Vratislav¹, L. Kalvoda¹, I. Medved², V. Kočí², R. Černý², F. Gašpar¹, J. Kukul¹, M. Kučeráková¹

¹Faculty of Nuclear Sciences and Physical Engineering, Czech Technical University in Prague, Prague, Czech Republic

²Faculty of Civil Engineering, Czech Technical University in Prague, Prague, Czech Republic
zelenji8@cvut.cz

Abstract

Safe long-term storage of radioactive waste requires barrier materials that limit liquid transport and radionuclide migration. As a low-CO₂ alternative to Portland cement, geopolymers made from recycled ceramic fines are promising candidates. This study investigates diffusion in such geopolymer concrete using neutron imaging at the LVR-15 reactor. Four media were tested: pure H₂O, pure D₂O, and 20 wt.% Gd(NO₃)₃ solutions in H₂O and D₂O. Neutron imaging enabled direct visualization of fronts and calculation of anisotropic diffusion coefficients (D_x , D_z) via Fick's law. Pure H₂O diffused fastest ($v \approx 12.5 \text{ mm} \cdot \text{h}^{-1}$; $D_x \approx 1.66 \times 10^{-12}$, $D_z \approx 5.33 \times 10^{-12} \text{ m}^2 \cdot \text{s}^{-1}$), followed by D₂O ($v \approx 3.45 \text{ mm} \cdot \text{h}^{-1}$; $D_x \approx 1.87 \times 10^{-12} \text{ m}^2 \cdot \text{s}^{-1}$, $D_z \approx 1.73 \times 10^{-12} \text{ m}^2 \cdot \text{s}^{-1}$). Gd(NO₃)₃ solutions were slower and exhibited two waves: for H₂O+Gd(NO₃)₃, $v \approx 10.5$ and $3.95 \text{ mm} \cdot \text{h}^{-1}$ ($D_x \approx 0.87\text{--}1.12 \times 10^{-11} \text{ m}^2 \cdot \text{s}^{-1}$, $D_z \approx 0.89\text{--}1.22 \times 10^{-11} \text{ m}^2 \cdot \text{s}^{-1}$); for D₂O+Gd(NO₃)₃, $v \approx 0.934/0.043 \text{ mm} \cdot \text{h}^{-1}$ ($D_x \approx 6.12\text{--}8.65 \times 10^{-13} \text{ m}^2 \cdot \text{s}^{-1}$, $D_z \approx 7.37\text{--}9.53 \times 10^{-13} \text{ m}^2 \cdot \text{s}^{-1}$). Vertical coefficients exceeded horizontal ones, indicating mild anisotropy. Direct observation of D₂O ingress is reported for the first time. These findings confirm the potential of geopolymers for nuclear waste barriers and demonstrate neutron imaging as a powerful tool for transport studies.

Keywords: neutron imaging; diffusion; Fick's law; geopolymer; transport coefficients.

Introduction and Motivation

Reducing greenhouse-gas emissions in construction motivates the search for cement-free binders with a smaller embodied carbon footprint than ordinary Portland cement (OPC). Geopolymers—alkali-activated aluminosilicate binders formulated from industrial by-products such as brick waste—offer comparable mechanical performance and chemical stability while substantially lowering CO₂ emissions associated with clinker production. In nuclear waste repositories, cementitious or cement-free mineral matrices act as a part of multi-barrier systems. Their effectiveness hinges on the kinetics of liquid ingress and solute transport, which control radionuclide mobility. While water ingress into concretes has been widely studied, reliable, spatially and temporally resolved measurements in geopolymer matrices, especially for heavy water and strongly absorbing solutes, remain scarce. Neutron imaging is particularly well-suited to study water transport because neutron attenuation is strongly sensitive to certain nuclides: protium has a large scattering cross section, deuterium and oxygen are comparatively weak scatterers/absorbers, and gadolinium exhibits an extraordinarily large absorption cross section for thermal neutrons. These contrasting cross sections can be exploited to enhance contrast and to trace diffusion with high fidelity. In this work, we leverage these properties to quantify diffusion dynamics in a recyclable, ecological geopolymer mortar designed for barrier applications [1].

Materials and Methods

Geopolymer mortar was prepared from recycled ceramic powder (0–0.125 mm; $d_{50} \approx 10.48 \mu\text{m}$) obtained from brick manufacturing as the precursor, activated by sodium water glass (silicate modulus 1.6) in combination with NaOH. The mixture dosage per batch comprised: ceramic powder 403 g, siliceous sand 1097 g, water 152 mL, sodium water glass 175 g, and sodium hydroxide 22 g. Fresh mixes were cast into six prismatic samples ($20 \times 20 \times 100 \text{ mm}$ – Figure 1), covered for 24 h to avoid early-age drying, demolded, and stored under laboratory conditions. Helium pycnometry and bulk density yielded a pore volume of $\sim 0.039 \text{ cm}^3 \cdot \text{g}^{-1}$ after 28 days; XRD/XRF revealed $\sim 47\%$ amorphous content with α -quartz, illite, biotite, and feldspars as major crystalline phases.

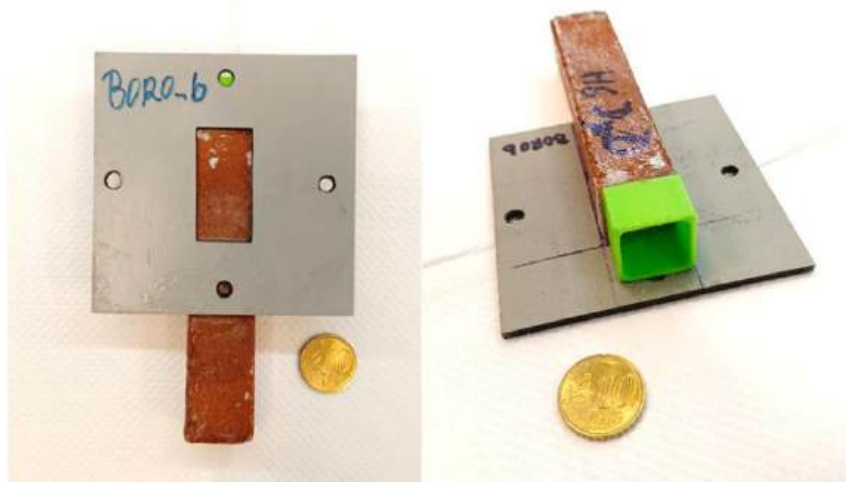


Figure 1. An example of the investigated samples with the boron-plastic screen (grey) and the water tank (green).

Diffusion media were: (i) pure H_2O , (ii) pure D_2O , (iii) $\text{H}_2\text{O} + \text{Gd}(\text{NO}_3)_3$ (20 wt.% Gd; denoted Gd+ H_2O), and (iv) $\text{D}_2\text{O} + \text{Gd}(\text{NO}_3)_3$ (20 wt.% Gd; Gd+ D_2O). Lateral faces of each specimen were sealed with epoxy to enforce predominantly one-dimensional through-thickness transport. Samples were mounted behind a rectangular boron-plastic aperture ($17 \times 35 \text{ mm}$) with a small liquid reservoir on the top surface to maintain a constant source boundary during the experiment. Neutron transmission imaging was performed on the KSN-2 neutron diffractometer at the LVR-15 reactor (Řež, Czech Republic) using a monochromatic thermal beam ($\lambda = 0.1362 \text{ nm}$) formed by a Cu(200) monochromator and Soller slits. Images were recorded by an ILL NOG 190506 neutron camera (Atik VS60 CCD, $2750 \times 2200 \text{ px}$, 16-bit grayscale). Raw frames were cropped, corrected for dead/bad pixels, and denoised (median filter). Line-spread analysis indicated an effective spatial resolution of 0.5–0.55 mm. Beam inhomogeneities in both vertical and horizontal directions were removed by normalizing each frame to the first frame of the series and to the actual exposure time (50–190 s).

Assuming small convective contributions and concentration-independent diffusivity over the observed ranges, the temporal change in path-integrated neutron absorption $A(x,z,t)$ was modeled by the 2D form of Fick's second law:

$$\frac{\partial A}{\partial t} = D_x \frac{\partial^2 A}{\partial x^2} + D_y \frac{\partial^2 A}{\partial y^2}$$

Spatial and temporal derivatives were approximated by finite differences at each pixel and time step, and the overdetermined linear system was solved in the least-squares sense to retrieve D_x and

D_z . Front positions were parameterized using the error-function solution for an infinite diffusion couple:

$$A(x, t) = \frac{1}{2} \left[1 - \operatorname{erf} \left(\frac{x - x_0}{2\sqrt{Dt}} \right) \right]$$

where x_0 denotes the interface position. Its time derivative $v = dx_0/dt$ was used to estimate wave velocities in the vertical direction. To reduce edge effects, only interior pixels were used [1].

Results

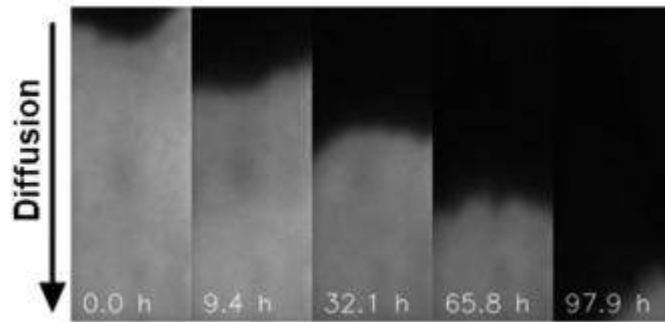


Figure 2. Neutron transmission images documenting the time evolution of diffusion, obtained for sample 6 with a diffusion of Gd+D₂O. The actual diffusion time is shown.

Time-lapse transmission maps revealed rapid ingress of pure water (H₂O) and heavy water (D₂O), while Gd-bearing solutions progressed substantially more slowly. In Gd+H₂O and Gd+D₂O, two distinct diffusion waves emerged along the vertical axis shortly after the start of the experiment (Figure 2); both advanced with nearly constant velocities over tens to hundreds of hours. For Sample 3 (Gd+H₂O), the fast/slow waves propagated at $v \approx 10.5$ and 3.95 mm·h⁻¹, respectively; for Sample 5 (Gd+D₂O), at $v \approx 0.934$ and 0.043 mm·h⁻¹. In contrast, single-wave behavior characterized the pure liquids, with H₂O $v \approx 12.5$ mm·h⁻¹ and D₂O $v \approx 3.45$ mm·h⁻¹. Direct visualization of D₂O ingress into the geopolymer matrix was achieved, with a modest increase in neutron transmission consistent with reduced scattering upon pore filling by heavy water.

Diffusion coefficients derived from the 2D Fick analysis showed a small but consistent anisotropy with $D_z > D_x$ across all media. Representative values (m²·s⁻¹) include: for H₂O, $D_x \approx 1.66 \times 10^{-12}$ and $D_z \approx 5.33 \times 10^{-12}$ m²·s⁻¹; for D₂O, $D_x \approx 1.87 \times 10^{-12}$ m²·s⁻¹ and $D_z \approx 1.73 \times 10^{-12}$ m²·s⁻¹; for Gd+H₂O, $D_x \approx (0.87-1.12) \times 10^{-11}$ m²·s⁻¹ and $D_z \approx (0.89-1.22) \times 10^{-11}$ m²·s⁻¹; for Gd+D₂O, $D_x \approx (0.612-0.865) \times 10^{-12}$ m²·s⁻¹ and $D_z \approx (0.737-0.953) \times 10^{-12}$ m²·s⁻¹. Velocities remained effectively constant within the observed time windows, supporting the assumption of concentration-independent D within each phase of the experiment [1].

Discussion

The split of the Gd-bearing fronts into two waves is consistent with dissociation of Gd(NO₃)₃ into a metal-containing cationic complex and nitrate anions that experience distinct interactions with the pore network and the geopolymer surface, leading to different effective mobilities. Because the two waves overlap in the absorption signal, the current inversion assumes a common D for both waves in the least-squares reconstruction; future work will target decoupled identification using multi-spectral or tracer-specific approaches. The mild anisotropy ($D_z > D_x$) likely reflects the combined influence of gravity-driven redistribution and anisotropic capillary rise at early

times; however, given that imaging started after initial wetting and that transport at late times is diffusion-dominated, the Fickian framework remains appropriate for recovering order-of-magnitude accurate coefficients. Importantly, the obtained D values in the geopolymer (10^{-12} – 10^{-11} $\text{m}^2\cdot\text{s}^{-1}$) are 1–3 orders lower than typical water-transport coefficients reported for OPC concretes under comparable conditions, supporting the suitability of the tested ecological mortar for barrier functions. Method verification on a standardized concrete dataset yielded $(9 \pm 4) \times 10^{-8}$ $\text{m}^2\cdot\text{s}^{-1}$, in reasonable agreement with literature, lending confidence to the inversion workflow. Uncertainties stem from spatial resolution (~ 0.5 mm), single-use specimens (no repetition per mix), and the neglect of concentration dependence of D . Nevertheless, internal cross-checks—solving the overdetermined system across multiple time windows—indicated solution stability within ~ 5 – 10 %. Future work will aim at: (i) separating ionic contributions to the two-wave propagation, (ii) testing temperature and saturation effects, and (iii) extending to larger sample sets with controlled porosity distributions.

Conclusions

Neutron imaging provides a high-fidelity, non-destructive window into water and salt transport in low-carbon geopolymers. We directly observed D_2O diffusion and quantified anisotropic diffusion coefficients and front velocities for H_2O , D_2O , and $\text{Gd}(\text{NO}_3)_3$ solutions. The emergence of two waves in Gd-bearing media highlights the role of ionic speciation in transport kinetics. Overall, the brick-recyclate geopolymer shows comparatively slow transport, underpinning its promise for nuclear-waste encapsulation and broader durability-critical applications in sustainable construction.

References

- [1] ZELENKA, Ján; DRÁB, M.; VRATISLAV, S.; KALVODA, L.; MEDVEĎ, Igor et al. Diffusion dynamics in ecological concrete studied by neutron imaging method. Online. *Journal of Sustainable Cement-Based Materials*. 2025, p. 1-10. ISSN 2165-0373. doi: 10.1080/21650373.2025.2486707. [cit. 2025-11-03].

Acknowledgements

This research was supported by the Czech Science Foundation (GAČR) under project No. 22-03474S and by the Grant Agency of the Czech Technical University in Prague (SGS) under grant No. SGS25/168/OHK4/3T/14. We also thank Jana Matoušková for determining the imaging resolution.

Obsah

Předmluva	1
Structure parameters of additively manufactured AlSi10Mg alloy (M. Endrych)	3
Quantum-like Model of a Rat in a Maze (A. Gaj)	9
Fatigue limit of additively manufactured materials (Š. Hortlík)	16
Atomic force microscopy (M. Jůza)	19
Gas pressure optimalization of titanium nitride thin films deposition by IJD method (M. Kolář)	25
Detekce laserového poškození pomocí odraženého He-Ne laserového záření (F. Novák)	30
A Hartree-Fock Analysis of Spherical Nanoparticles in the Jellium Approximation (M. Píro)	36
Preparation and analysis of multilayer metal- dielectric systems by PVD methods (J. Lis)	42
Úhlově rozlišená spektroskopie Brillouinova-Mandelštamova rozptylu světla pro měření elastické anizotropie safíru (Z. Soudná)	48
Diffusion Dynamics in Ecological Concrete Studied by Neutron Imaging (J. Zelenka)	54

Autor (editor): K. Aubrechtová , L. Kalvoda, M. Kučeráková

Název díla: **Sborník příspěvků 14. studentské vědecké konference fyziky pevných látek, fotoniky a materiálů**

Praha 2025

Vydalo: České vysoké učení technické v Praze

Zpracovala: Fakulta jaderná a fyzikálně inženýrská

Kontaktní adresa: Trojanova 13, 120 00 Praha 2

Tel.: +420 22435 8621

Tisk: powerprint s.r.o.

Adresa tiskárny: Zikova 17, 160 00 Praha 6 - Dejvice

Počet stran: 59 Náklad: 15 kusů Pořadí vydání: první